



**HAL**  
open science

# Effect of temperature, rate, and molecular weight on the failure behavior of soft block copoly(ether–ester) thermoplastic elastomers

Simone Sbrescia, Jianzhu Ju, Costantino Creton, Tom Engels, Michelle Seitz

## ► To cite this version:

Simone Sbrescia, Jianzhu Ju, Costantino Creton, Tom Engels, Michelle Seitz. Effect of temperature, rate, and molecular weight on the failure behavior of soft block copoly(ether–ester) thermoplastic elastomers. *Soft Matter*, 2023, 19 (27), pp.5127-5141. 10.1039/D3SM00210A . hal-04266871

**HAL Id: hal-04266871**

**<https://hal.science/hal-04266871>**

Submitted on 4 Nov 2023

**HAL** is a multi-disciplinary open access archive for the deposit and dissemination of scientific research documents, whether they are published or not. The documents may come from teaching and research institutions in France or abroad, or from public or private research centers.

L'archive ouverte pluridisciplinaire **HAL**, est destinée au dépôt et à la diffusion de documents scientifiques de niveau recherche, publiés ou non, émanant des établissements d'enseignement et de recherche français ou étrangers, des laboratoires publics ou privés.

# Effect of Temperature, Rate, and Molecular Weight on the Failure Behavior of Soft Block Copoly(ether-ester) Thermoplastic Elastomers

Simone Sbrescia<sup>1</sup>, Jianzhu Ju<sup>2</sup>, Costantino Creton<sup>2</sup>, Tom Engels<sup>3</sup>, Michelle Seitz<sup>3</sup>

<sup>1</sup> Bio and Soft Matter Division (BSMA), Institute of Condensed Matter and Nanosciences (IMCN), Université Catholique de Louvain, B-1348 Louvain-la-Neuve, Belgium;

<sup>2</sup> Laboratoire Sciences et Ingénierie de la Matière Molle, ESPCI Paris, PSL University, CNRS, Sorbonne Université, Paris, France;

<sup>3</sup> DSM Materials Science Center, Urmonderbaan, 6167 RD Geleen The Netherlands;

## Abstract

Thermoplastic elastomers (TPEs) based on multiblock copolymers are an important class of engineering polymers. They are widely used in many applications where flexibility and durability are required and are seen as a sustainable (recyclable) alternative to thermoset rubbers. While their high-temperature mechanical behavior has received recent interest, few studies have explored their fracture and fatigue behavior. Understanding how the temperature and rate-dependence of the deformation behavior at both a local and global scale influences the fatigue resistance and failure behavior is critical when designing with these materials. In this study, the failure behavior in tensile, fracture, and fatigue of well-characterized, industrially relevant, model block copoly(ether-ester) based TPEEs were evaluated over a wide range of temperatures, deformation rates, and molecular weights. Small changes in temperature or rate are shown to result in a sharp transition between a highly deformable and notch resistant response, to a more brittle and strongly notch-sensitive response. This behavior surprisingly manifests itself as a threshold strain below which the cracks do not propagate in fatigue and increasing deformation rates decreases the materials toughness in fracture tests, whereas in tensile tests the opposite is observed. The change from homogenous to inhomogeneous stress fields for tensile and fracture experiments coupled with the viscoelasticity and strain-dependent morphology of TPEs explains why a different rate dependency is observed. Strain and stress delocalization is key to achieve high toughness. Digital Image Correlation is used to measure the size and time dependence of the process zone. Comparison with micromechanical models developed for soft, elastic, and tough double network gels highlights the dominance of high strain properties for toughness and explains the strong molecular weight dependence. However, to understand the rate dependence, the characteristic times for stress transfer from the crack tip and the time to nucleate failure must be compared. The results presented in this study demonstrate the complex effect of loading conditions on the intrinsic failure mechanisms of the TPE material, and provide a first attempt at rationalizing that behavior.

## Introduction

Thermoplastic elastomers (TPEs) based on multiblock copolymers offer a sustainable alternative to rubbers as they are crosslinked via physical associations and trapped entanglements that lead to a high level of reversible elasticity coupled with melt processability [1]. Despite being widely used in applications where high resilience and fatigue resistance are key, such as automotive ducts and shoe soles, only recently have studies begun to explore their crack propagation properties in monotonous loading and cyclic fatigue conditions. We are not aware of previous studies exploring temperature and rate dependence in this context. Understanding how the temperature (T)- and strain rate dependence of the deformation behavior at both a local and global scale influences the fatigue resistance and failure behavior is critical when designing parts made from soft and tough materials such as TPEs.

Soft -TPEs show similar complex fracture behavior as other soft and tough materials [2-6]. The fracture toughness of soft polymer networks stems from the energy dissipated in a process zone around the crack tip [2]. Double network (DN) hydrogels are remarkable examples of materials that maximize the use of this mechanism [2, 3, 7-11]: the energy dissipation due to sacrificial bond scission provides the materials with a fracture energy  $\Gamma$  several orders of magnitude higher than the corresponding single network. Introducing crystal domains that can undergo plastic deformation is another way to improve both the toughness and the fatigue resistance [12]. Indeed, any kind of irreversible damage during the first loading, often referred to as the Mullin's effect [13], potentially increases the toughness, but not necessarily fatigue resistance [3, 14, 15]. In addition to the presence of a dissipating mechanism, the local volume over which this deformation and dissipation occurs is critical to determine the notch-resistance of a material [2, 9, 11, 16]. The presence of network imperfections, strain hardening, or the introduction of fibers as reinforcement are proven to increase the volume in which the local stresses and strains at the crack tip delocalize and stabilize during deformation [6].

Understanding these dissipation mechanisms and how much energy the material can store elastically is critical for interpreting fracture tests, as it is only the elastically stored energy that causes crack propagation [2, 16, 17]. Mzabi *et al.* [16] and Mayumi *et al.* [17] introduced the idea that to estimate the actual energy available for crack growth,  $g_{local}$ , the energy release rate,  $G$ , should be scaled by the ratio of elastically stored energy to total applied work,  $\alpha$ , resulting in

$$g_{local} = \alpha G. \quad (1)$$

The deformation behavior of TPEs is characterized both by a dissipating mechanism and strain hardening [18-20] resulting in high toughness and fatigue resistance [3, 9]. Despite absorbing considerable energy during loading, they remain highly elastic upon unloading. Both the dissipating and strain hardening mechanisms stem from the strongly deformation-dependent large strain morphology of TPEs [19, 21-32]. Briefly, the initial microstructure of TPEs based on multiblock copolymers is characterized by an interlocking network of rigid, hard block (HB) domains providing the material with a higher initial elastic modulus [18, 20]. Upon stretching, the HB domains progressively break up and align in the stretching direction along with the amorphous phase. The breakup is a significant source of energy dissipation, as shown by hysteresis tests [5, 18-20], and may result in a changing modulus with strain that initially shows a decrease in modulus, transitioning into an increase upon large deformation. Additionally, the orientation of the polymer chains along the stretching direction results in strain-hardening [5, 18, 20, 33], which helps to homogenize the stresses and to increase the size of the process zone [9]. For polyether based multiblock copolymer TPEs, chain orientation can also result in strain induced crystallization (SIC) of the soft blocks (SBs) which has a dramatic influence on the mechanical response [4, 5, 20, 33, 46]. Scetta *et al.* showed that thermoplastic polyurethanes (TPUs), a widely used class of TPEs, can achieve fatigue threshold one order of magnitude higher than crosslinked rubbers [4]. They attributed this high fatigue threshold to the microstructural reorganization occurring at the crack tip during loading, providing the material with a self-stiffening mechanism that shields the crack tip and reduces the intensity of the strain concentration.

Despite being extremely tough at lower temperatures, many soft multiblock copolymer TPEs show a decrease in the energy required for fracture in continuous tensile loading with increasing temperature (T) [20, 34-38]. This behavior limits the range of applications where TPEs can be used as well as their suitability for some processing technologies at  $T >$  room temperature (RT). This

decrease is believed to originate from the T- and rate-dependent kinetics of the associations between HBs [34, 20] and from a decreasing crystalline volume fraction with increasing T [35].

The failure mechanism of these copoly(ether-ester) multiblock copolymers was first addressed by Aime et al. [34], who described failure in terms of connectivity loss of the associated hard block network. This occurs when the fraction of chains connected to the HB network falls below the percolation threshold. The T- and stress-activated HB pull-out from the crystals occurring during deformation progressively decreases the fraction of connected chains until it drops below this percolation threshold and the sample fails by localized creep.

Consistent with this model, increasing the total chain molecular weight (Mw) has been shown to improve the T resistance with little influence on small-strain mechanics. Increasing Mw increases the failure strain and the strain hardening [20, 32, 34, 37, 39]. However, failure of samples in uniaxial tension does not occur by macroscopic flow but by the nucleation of local defects in the initially homogeneous sample that propagate then as cracks. Thus, to understand failure it is necessary to investigate what happens in regions of high stresses and strains where failure initiates. This is why we focus on fracture and fatigue tests where notches introduce stress concentrations.

This work uses industrially relevant model copoly(ether-ester) (TPEEs) with 30 wt% of hard blocks (HB) whose mechanical properties have been extensively characterized [20, 21, 34-36, 43]. They have a room temperature (RT) modulus of  $\sim 25$  MPa [20] with high extensibility and elasticity due to the crystallized HBs acting as physical crosslinks. As the HBs in these systems are characterized on average by only a few PTB monomeric units ( $\sim 4.5$  [20]), crystallization is not characterized by folding of the HBs into crystalline lamellae, but rather by parallel stacking of the crystallizing HBs forming eventually long “ribbon-like” crystals of height and thickness comparable to the HB length [26,35]. The HB length distribution is one of the main contributing factors in determining the melting temperature of the PBT crystals in these materials [35], which is generally lower than the one of pure PBT. Indeed, the materials tested in this paper are characterized by a melting peak temperature of  $\sim 175$  °C. Due to the combined effect of stress, time, and temperature, stacked HBs belonging to different polymer chains can be easily pulled-out from the ribbons they are attached to, making these materials behaving as transient networks [34]. Figure S1 summarizes the molecular structure and crystallinity of this systems. We perform fracture and fatigue tests on notched, pure shear samples commonly used to evaluate the fracture energy of both soft and tough materials [2, 4, 5, 40, 41] and for cyclic fatigue experiments. Surprisingly, we observe a sharp threshold for fracture and fatigue crack propagation that depends on rate, temperature, and Mw. Additionally, we observe an opposite rate dependence for toughness in unnotched versus notched samples.

We begin with a description of the TPEEs and the testing methods used. Next, we show the results from tensile, fatigue, and fracture tests performed at different testing conditions. Then analysis of the crack shape and propagation speed are presented along with crack tip strain field evaluation using Digital Image Correlation (DIC). We explore if the models developed to explain the high toughness of DN gels [8, 11, 42] capture the key variables contributing to toughness of our system. Finally, a mechanistic picture is proposed that rationalizes the apparently contradictory results obtained with different testing geometries and conditions by considering the balance of the timescales for delocalization and failure initiation versus loading rate.

## **Materials and methods**

### ***Materials***

The model TPEE used is a poly(ether-ester) multiblock copolymer based on polybutylene terephthalate (PBT) as HB and poly(tetramethylene oxide) (PTMO) as soft block (SB) obtained via transesterification followed by polycondensation of dimethyl terephthalate (DMT), 1,4-butanediol (BDO), and PTMO diol. Details on the synthesis procedure have been previously described [43]. The samples are made of 30 wt% of HB, and with SB with an average length of 2 kg/mol. Two different total chain (weight average) Mw's are tested: 33 and 76 kg/mol, which we refer to as low- and high-Mw, respectively. These materials have been studied previously and correspond to samples labeled 70\_PTMO2k\_33 and 70\_PTMO2k\_76 in ref. [20]. Note that at RT, the SBs undergo strain-induced crystallization in uniaxial tension (SIC) [20, 33, 46]. Since the  $T_m$  of the SIC SBs is around  $\sim 50$  °C, we do not expect SIC for the tests at higher  $T$ 's. For this reason, the test at  $T > RT$  are performed starting at a temperature of  $T = 75$  °C, to ensure that SIC does not occur during the test.

### **Mechanical Tests**

For clarity, an overview of the different sample geometries and test protocols for the tensile, fatigue, and fracture tests are given in Fig S2 in the Supplementary Information.

### **Standard and cyclic tensile tests**

Tensile bars of ISO 527/5A standard shape are cut out from 200  $\mu\text{m}$  thick, hot-pressed films and tested on a standard Zwick Roell (Germany) 1474 Universal tensile testing machine equipped with an air circulation oven. The sample preparation and tensile test procedures for standard and cyclic loading follows the same methodology described in [1]. The nominal, or engineering strain ( $\epsilon$ ) is determined using an optical extensometer for increased accuracy. The rate of deformation in all tests is applied as a constant engineering strain rate, meaning that the Henky strain rate during testing is continuously decreasing. The applied stretch or draw ratio,  $\lambda$ , is easily derived from the engineering strain,  $\epsilon$ :  $\lambda = 1 + \epsilon$ . The volumetric toughness calculated from tensile tests,  $W$ , corresponds to the integral of the stress-strain curve, i.e.:

$$W = \int_0^{\epsilon_f} \sigma d\epsilon, \quad (2)$$

where  $\sigma$  is the engineering stress and  $\epsilon_f$  the failure strain.

Cyclic tensile tests are performed at a nominal engineering strain rate ( $\dot{\epsilon}$ ) of  $0.017 \text{ s}^{-1}$  and unloaded at  $0.17 \text{ s}^{-1}$ . The applied strain on the first cycle is 50% while the following deformation steps are of 100% in strain. The lower strain rate during loading is chosen to allow the machine to properly switch direction when the target strain of each cycle is reached. The rate is changed upon unloading, corresponding to the fastest crosshead displacement speed achievable by the machine (500 mm/min) to get as close as possible to the high rates at which the elastic energy is released during crack propagation.

The elastically-stored energy,  $W_{el}$ , is calculated by integrating the unloading curves, i.e., as in Equation 2, but using as integration limits the appropriate strains reached upon loading and unloading. The dissipated energy,  $W_p$ , is calculated as  $W - W_{el}$ .  $E_1$  and  $E_2$  are the moduli on unloading at high and low strain, respectively, calculated in analogy to the work of Tanaka *et al.* [8, 9], as the slope of the unloading stress-strain curve at the end and at the beginning of the unloading step. See Figure S2 for a schematic description. The ratio between the total and the elastic energy or relative elasticity,  $\alpha$ , is calculated using

$$\alpha = \frac{W_{el}}{W} = \frac{W_{el}}{W_{el} + W_p}. \quad (3)$$

## **Fatigue tests**

Rectangular samples  $50 \times 5 \times 1 \text{ mm}^3$  of the low Mw sample were injection molded at the Laboratoire de Recherche et Contrôle des Caoutchoucs et Plastiques (LRCCP) with a BOY 50 M injection molding machine. Sample shape includes two thicker sections to allow clamping in cyclic testing as shown in Figure S2. For all the tests, the frequency of cyclic loading is 10 Hz and the samples are unloaded to  $\varepsilon = 10\%$  to avoid buckling. Propagation of the crack was detected with a digital camera (BAUMER VCXU-32M) equipped with a macro-objective (pixel size  $38 \mu\text{m}$ ). The cyclic loading of a notched specimen is shown in Figure S2. With width being much larger than the initial length and crack length, the stretched part of the sample is under pure-shear loading [4].

The fatigue tests are performed at different temperatures, from RT to  $100 \text{ }^\circ\text{C}$ . For tests at RT, the following protocol was used. First, an accommodation step where the unnotched sample is cycled  $\sim 4 \times 10^4$  times between  $\varepsilon = 10$  and  $60\%$  to eliminate the Mullins and other transient effects [2, 16]. The sample is unloaded to  $\varepsilon = 10\%$  and not to  $\varepsilon = 0\%$  to avoid buckling during unloading [4]. Then, the sample is notched with a razor under a strain of  $10\%$  (initial crack length around 5 mm). Finally, the notched sample is sinusoidally cycled between  $\varepsilon = 10\%$  and an increasing value of the maximum amplitude strain at a frequency of 10 Hz for up to  $10^6$  cycles. At  $T > \text{RT}$ , the samples are fatigued between  $\varepsilon = 10\%$  and the maximum amplitude strain without any accommodation prior to notching. The primary cause of the latter is mainly due to the inability to attain complete accommodation at elevated temperatures in these transient networks at elevated temperatures.

At RT, the energy release rate is calculated from an unnotched sample using:

$$G_c = hW(\varepsilon_{max}) \quad (4)$$

where  $h$  is the initial height of the unstretched sample (5 mm) and  $W(\varepsilon_{max})$  is the strain energy density as a function of the maximum applied strain,  $\varepsilon_{max}$ , calculated as in Equation 2 [44].

## **Fracture tests using pure-shear rectangular samples and continuous loading**

For the fracture tests, the samples of  $60$  (or  $30$ )  $\times 5 \times 0.2 \text{ mm}^3$  with a 15 (or 10) mm notch were used. To avoid slippage in the grips, the sample is glued between 1 mm thick plates of a similar TPEE in the grips. Prior to mounting the sample in the grips, a notch is introduced with a sharp razor blade. Due to the high stability of the crack tip below a critical displacement, it is not possible to perform steady-state crack propagation experiments, e.g. where the sample is rapidly loaded to a fixed displacement prior to crack propagation. Instead, samples were continuously loaded at a fixed cross-head displacement speed. The tests are performed at  $T$  between RT and  $150^\circ\text{C}$  and engineering strain rates,  $\dot{\varepsilon}$ , between  $0.0017$  and  $1.7 \text{ s}^{-1}$  as indicated in the text and figures. The fracture toughness calculated from fracture tests,  $\Gamma$ , is calculated by

$$\Gamma = h \int_0^{\varepsilon_f} \sigma d\varepsilon, \quad (5)$$

where the unnotched cross-section is used to calculate the stress ( $\sigma$ ).

Videos of the propagating crack are collected with an NR4-S3 high-speed camera (IDT vision, USA) set to 3000 fps. Only when the crack propagates perpendicular to the stretching direction is the crack propagation speed calculated using ImageJ (National Institute of Health, USA). While the samples experience continuous loading, the crack propagation speeds observed are  $\sim 2$  orders of magnitude higher than the maximum crosshead-displacement speed ( $\sim 8 \text{ mm/s}$ ). Thus, we believe a comparison can still be made to crack speeds measured on other systems using steady-state crack propagation experiments.

## Digital Image Correlation (DIC)

We collected images during fracture tests at different nominal strain rates for  $60 \times 10 \times 0.2 \text{ mm}^3$  samples with 10 mm notch length and calculated the space resolved strain with digital image correlation (DIC). Images are collected by a CMOS camera (BASLER acA2000-340km, Germany) at 100 frames/s with pixel size of 0.02 mm/pixel and the surface of the sample is prepared by spray painting. The processing is done using the open source pyDIC program developed by Damien André [45]. Local strain distribution in undeformed coordinate ( $\epsilon_{xx}$ , corresponding to parallel and perpendicular to the stretching direction) are calculated in adjacent images and summed to obtained reliable strain at large deformation. Grid size is  $0.12 \text{ mm} \times 0.12 \text{ mm}$  (6 pixels).

## Results

### Standard and cyclic tensile tests: effect of $T$ , strain rate ( $\dot{\epsilon}$ ), and Mw on toughness ( $W$ )

The deformation behavior is similar among the different testing conditions. Figure 1a shows a representative example. Additional examples are given in Figure S3. Briefly, the stress increases roughly linearly to  $\sim 10\%$  strain. Then, the slope begins to decrease which we attribute to plastic deformation (yielding) of the crystalline domains of PBT. Next, the stress mildly increases to  $\sim 300\%$  strain when the material starts to harden. Finally, high stresses and strains are reached resulting in breakage.

Both samples are characterized by a decreasing  $W$  with increasing  $T$ , as shown in Figure 1-b. This not only results from a decrease of the overall stress level, but also from a decrease of the strain at break ( $\epsilon_f$ ) with increasing  $T$  (Figure 1-c). The effect of  $T$  on  $\epsilon_f$  is stronger for the low-Mw sample, consistent with previous observations [20, 34, 36-38]. This behavior has been rationalized by Aime *et al.* [34] by treating the material as a transient network and considering the rate and  $T$  dependence of the kinetics of the association between the HBs [34]. With increasing  $T$ , the HB disassociation rate increases, leading to a faster loss of network connectivity. Additionally, increasing  $T$  progressively decreases the crystallinity [36], which significantly influences the overall stress response [20, 36, 47]. The transient nature of the crosslinks responsible for the strong  $T$  dependence also leads to a weaker rate dependence. Previous works [20, 34] show that  $\epsilon_f$  increases with increasing  $\dot{\epsilon}$ . Increasing  $\dot{\epsilon}$  leads to a slightly higher  $W$  as shown in Figure 1-b's insert.

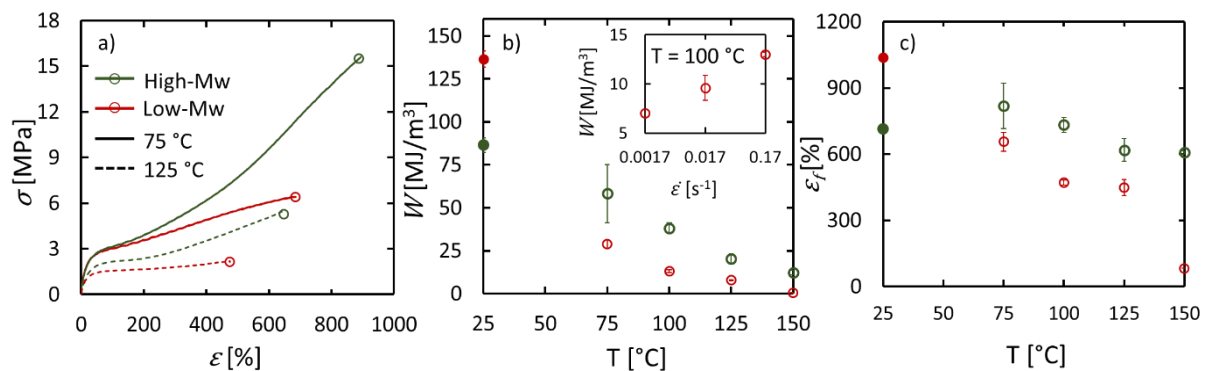


**Figure 1:** a) Representative engineering stress-strain curves from standard tensile tests with symbols indicating the point of failure. b) Toughness,  $W$ , calculated from equation 2 versus temperature for tensile tests at  $\dot{\epsilon} = 0.17 \text{ s}^{-1}$ . Insert shows  $W$  at  $100 \text{ °C}$  for three different  $\dot{\epsilon}$ 's. c) Strain at break,  $\epsilon_f$ , versus temperature for the same tests as shown in b). Data points where SIC of the SB is expected to occur are denoted with filled symbols.

At RT, the stress response is significantly influenced by the SIC of the SBs, which leads to a significant increase in strain hardening and decrease in the  $\varepsilon_f$  [20, Figure S3]. This is more pronounced for the high-Mw sample and results in the high-MW sample having lower  $W$  at RT than the low-MW. At  $T > RT$ , the high-Mw sample shows higher failure stresses ( $\sigma_f$ ) and  $\varepsilon_f$  leading to higher  $W$ . Longer chains have more HBs and entanglements per chains, which leads to a lower probability of disconnecting chains from the network and thus to an increased lifetime of the stress-bearing segments and associated larger high-strain elasticity [20, 36].

The relative elasticity,  $\alpha$ , is the ratio between the unloading (elastically stored) and the total energy absorbed during loading in a cyclic test. Figure 2 shows that  $\alpha$  is higher for the high-Mw sample at each applied strain. At RT,  $\alpha$  monotonically decreases with increasing strain. The fraction of SIC SB crystals increases with increasing deformation and, consequently, the overall plasticity of the system increases. At  $T > RT$ ,  $\alpha$  initially decreases due to the plastic deformation of the crystalline network, then it slightly increases before reaching a plateau value passed the yield point ( $\varepsilon > 50\%$ ). Interestingly,  $\alpha$  does not significantly change with  $T$  at temperatures where there is no SIC. The higher values of  $\alpha$  for high Mw at  $T > RT$  is consistent with enhanced elasticity for higher Mw.

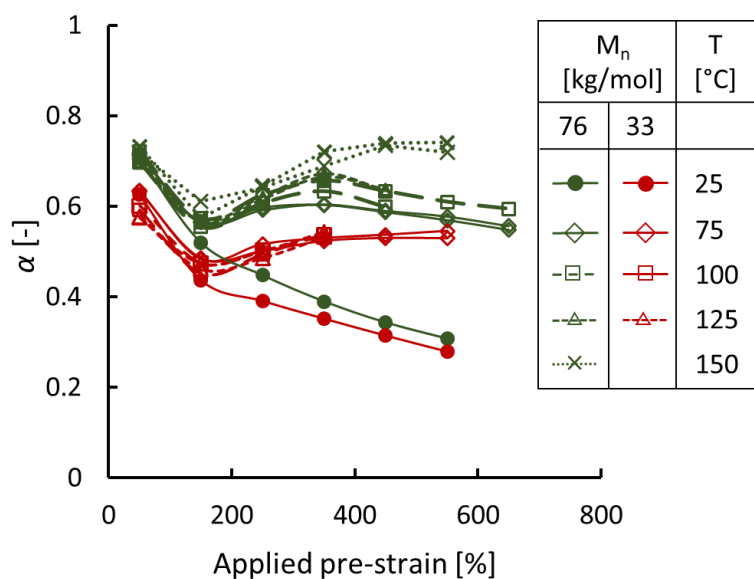


**Figure 2:** a) Relative elasticity,  $\alpha$ , versus applied pre-strain from cyclic tensile tests at different  $T$ 's for low and high Mw sample. Data points where SIC of the SB is expected to occur are denoted with filled symbols. The data point of  $M_n=33$  kg/mol at  $T=150$  °C is missing because the material fails before being able to complete a full stress-strain cycle.

To later compare the critical energy for crack propagation,  $g_{local}$ , with crack velocity, we need to scale the energy release rate  $G$  by  $\alpha$ . As our analysis will focus on the data at  $T > RT$ , where  $\alpha$  is roughly constant at applied strains above 50%, we will use the averaged values for  $\alpha$  of 0.6 and 0.5 for the high- and low-Mw samples, respectively. As we do not observe significant differences in  $\alpha$  with increasing  $T$ , we can expect negligible differences in  $\alpha$  when varying strain-rates. Hence, as a first approximation, we will use the same value of  $\alpha$  to estimate  $g_{local}$  for the fracture tests performed at different strain-rates.

To summarize the key aspects from the tensile evaluation, we observe that the toughness,  $W$ , decreases with increasing T due to a decrease of the overall stress levels and to a decrease of  $\varepsilon_f$ . At T > RT, increasing Mw leads to higher values of  $W$ , due to an increase in both  $\varepsilon_f$  and strain hardening due to increased network connectivity. SIC of the SB occurs at RT resulting in  $W$  decreasing with Mw and  $\alpha$  decreasing with strain. At all temperatures > RT,  $\alpha$  evolves with strain in similar ways for low and high Mw samples reflecting the breakup and chain-orientation of the crystals. The higher Mw samples show a higher relative elasticity at all conditions. At T > RT and at  $\varepsilon > 50\%$ ,  $\alpha$  is insensitive to changes in T and  $\varepsilon$ .

Next, we show the results from fatigue and fracture of notched samples where high stresses and strain are localized ahead of the notch and compare them with the results obtained from uniaxial tensile tests where the stress-strain field is homogeneous.

### ***Effect of T and strain amplitude on fatigue behavior***

Surprisingly, there appears to be a threshold strain below which the cracks do not propagate in fatigue. However, if the maximum strain exceeds the threshold strain, the crack rapidly propagates through the entire sample, i.e., the sample fails in just one cycle. Figure 3 maps the fatigue behavior for the low-Mw sample at different maximum applied strains and temperatures tested. Below the threshold strain (dashed line) no crack-propagation is observed after  $10^6$  cycles, meaning that the crack propagation speeds are at most  $\sim 0.05$  nm/cycle (the resolution limit of the images) or that the crack effectively blunts. Above the dashed line, the crack propagates rapidly upon reaching the target amplitude strain (1 cycle). The threshold line decreases with increasing T, similar to the toughness from tensile tests (Figure 1).

The results indicate a sharp transition from a notch-resistant material with virtually infinite lifetime to a strongly notch-sensitive one, triggered by small changes in T or applied strain. No conditions of stable fatigue crack growth were found meaning that the fatigue threshold ( $G_b$ , i.e. where no crack propagation is observed) equals the toughness ( $G_c$ , i.e. where the failure occurs in one cycle). At RT,  $G_c$  of the low-Mw sample is  $\sim 15$  kJ/m<sup>2</sup>. As a comparison, typical rubbers have a  $G_c$  more than 1 order of magnitude lower (40-100 J/m<sup>2</sup> [48, 49]) while typical values of  $G_c$  for SBR (< 5 kJ/m<sup>2</sup>) and for filled rubbers (< 10 kJ/m<sup>2</sup>) are only slightly lower. TPUs show a more similar fatigue behavior with very high fatigue threshold ( $\sim 5$  kJ/m<sup>2</sup>) and  $10 < G_c < 20$  kJ/m<sup>2</sup> [4, 5]. However, they do show a stable crack propagation regime contrary to the TPEE used in this study. Fatigue data at elevated temperatures on TPEs is found to be scarce. Scetta [50] did report fatigue data on a set of TPUs at 60°C which showed comparable fatigue performance as measured on those same systems at 23°C [4, 5]. This stable performance of the fatigue response over a temperature window of 23-60°C is comparable to what is found here for the TPEE systems where only at temperatures above 60°C we see the toughness decrease significantly.

At T > RT, cycling of un-notched samples was not performed. Therefore, we estimate  $G_c$  using  $G_c = hW_{el}(\varepsilon_{max} \sim 50\%)$ , where  $W_{el}$  is the area below the unloading stress-strain curve from the cyclic tensile tests on un-notched tensile bars (Figure 1). The values of  $G_c$  estimated in this way are  $\sim 11$  kJ/m<sup>2</sup> and  $\sim 8$  kJ/m<sup>2</sup> at 75 °C and 100 °C, respectively.

Since the fatigue behavior is strongly dominated by the morphological strain-induced transformations occurring in a local area around the crack tip [5], these results suggest that in the non-propagating region in Figure 3 the microstructure at the crack tip resulting from the first loading remains stable with repeating cycles. The results are consistent with previous hysteresis tests [19, 20], which showed a large amount of energy dissipated during the first cycle but little dissipation

during the subsequent cycles. Both results indicate a major microstructural transformation occurring in the material during the first loading that results in high stability and elasticity. Additionally, the higher elasticity and strain hardening of the stretched material at the crack tip likely contributes to the crack stability [3, 6] by delocalizing the stresses to a larger region ahead of the crack tip and, hence, avoiding damage accumulation at the crack tip.

To summarize, we observe a critical threshold strain below which the crack does not propagate in fatigue and above which the crack propagates fast through the whole sample in a single cycle. The critical strain amplitude corresponding to this threshold decreases with increasing  $T$ , similarly to the decrease in  $\epsilon_f$  observed in tensile tests. To better understand this transition from notch-resistant to notch-sensitive behavior in fatigue, we next explore the results from fracture tests performed at different  $T$ 's and  $\dot{\epsilon}$ 's under continuous stretching of notched samples to failure.

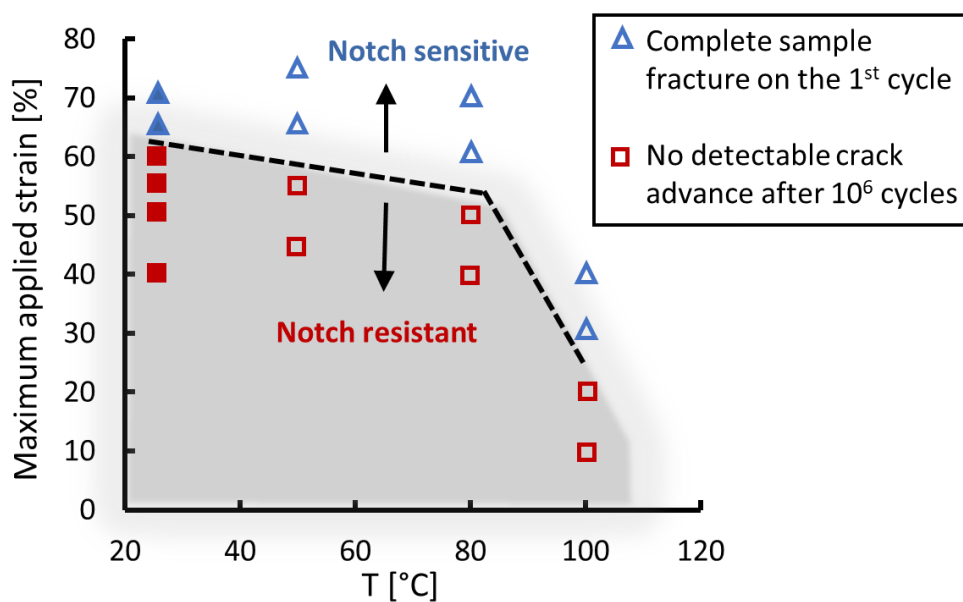


**Figure 3:** Map indicating conditions of applied strain and temperature where either no detectable crack propagation was observed (grey area) or failure was observed in one cycle (white area) for the low Mw sample. The dashed line is a guide to the eye showing the transition between the behaviors. Data points where SIC of the SB is expected to occur are denoted with filled symbols.

### **Fracture tests: effect of $T$ , strain rate ( $\dot{\epsilon}$ ), and Mw on the failure behavior**

In continuously loaded, constant nominal strain-rate fracture tests, we observe regions in which the material behaves as notch-resistant or notch-sensitive similar to the fatigue tests. Figure 4 maps the failure behavior of low- (a) and high- (b) Mw samples at different strain rates and temperatures. At the testing conditions falling in the gray region, the behavior of the crack is characterized by extreme blunting resulting in either the sample slipping from the grips or with a crack propagating parallel to the stretching direction as sometimes observed for filler natural rubber samples and called knotty tearing [51]. Above the dashed line, the crack propagates perpendicular to the stretching direction and the critical strain required for propagation depends on  $T$ ,  $\dot{\epsilon}$ , and Mw. Comparing the two maps, it is clear that increasing Mw increases the region of strain rates and temperatures where the material is notch-resistant.

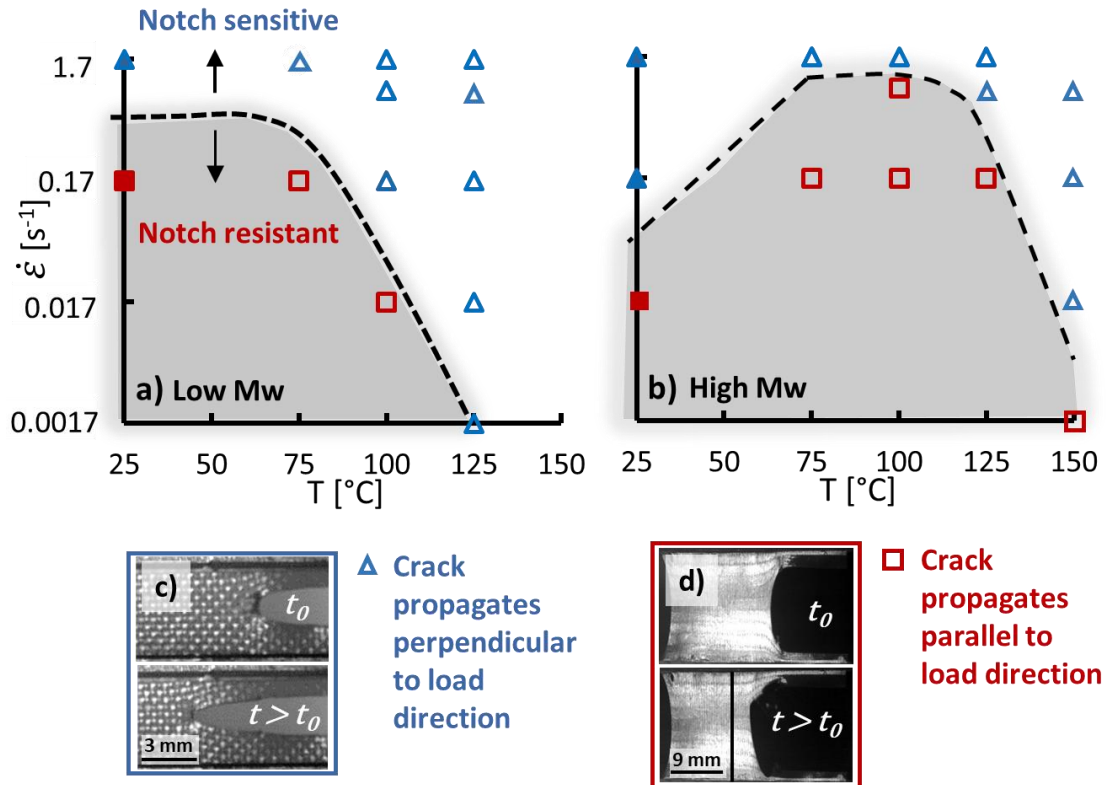


**Figure 4:** Map indicating regions of T and  $\dot{\epsilon}$  of different crack-propagation behavior for low- (a) and high- (b) Mw samples during continuously loaded fracture tests. Below the dashed line corresponds to the conditions where the material notch-resistant behavior with extreme blunting. Above it, notch-sensitive behavior is observed with cracks propagating perpendicular to the loading direction. The snapshots show examples of cracks propagating perpendicular (c) or parallel (d) to the loading direction corresponding to a low-Mw sample tested at 0.17 s<sup>-1</sup> and at temperatures of 100 °C and 75 °C, respectively.  $t_0$  indicates the instant before the crack propagation. Movies of the propagating crack relative to the experiments showed in c) and d) are present in the supplementary materials (Video 1 and Video 2, respectively). Data points where SIC of the SB is expected to occur are denoted with filled symbols.

When the crack propagates perpendicular to the loading direction, regardless of the testing conditions, failure occurs by first blunting i.e., by the formation of a highly stretched zone at the notch tip, followed by nucleation and propagation of smaller cracks originating in this region [52, 6]. In these cases, the fracture toughness,  $I$ , can be calculated using equation 5 from the area below the loading curves. Figure 5 shows  $I$  versus temperature for two nominal strain rates for low- and high-Mw samples. The values of  $I$  strongly depend on the testing conditions and fall between 1 and 100 kJ/m<sup>2</sup>. At RT with  $\dot{\epsilon} = 1.7$  s<sup>-1</sup>,  $I$  is 10-20 kJ/m<sup>2</sup>, which is between those of TPUs (10-100 kJ/m<sup>2</sup>) [4, 5] and classical rubbers (1-20 kJ/m<sup>2</sup>) [53]. Consistent with tensile tests,  $I$  decreases with increasing T. Additionally, the high-Mw sample shows higher  $I$  than the low-Mw for T > RT when compared at the same  $\dot{\epsilon}$ . At RT, there are no significant differences on  $I$  when varying Mw. This is attributed to the dominances of SIC at RT.

Strikingly, however, decreasing the strain rate in fracture tests increases the observed fracture toughness. Figure 6 directly compares the loading curves from tensile and fracture tests to highlight the contrasting behavior observed when comparing tests involving homogenous and inhomogeneous stress-strain fields.

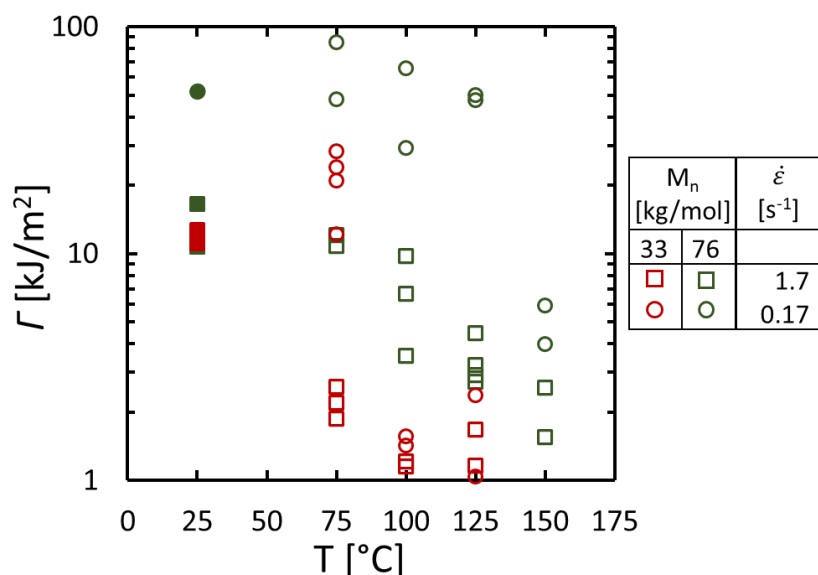


**Figure 5:** Fracture toughness,  $\Gamma$ , versus temperature for different Mw and strain rates noted in the legend. Values for  $\Gamma$  at the other testing conditions are given in Table S1. Data points where SIC of the SB is expected to occur are denoted with filled symbols.

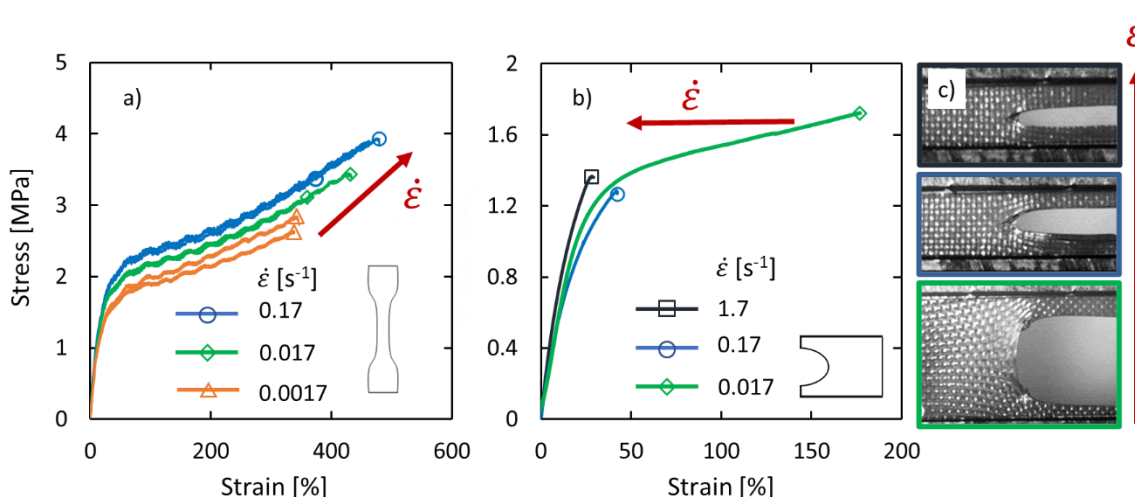


**Figure 6:** Engineering stress-strain curves for a low-Mw sample from tensile (a) and fracture (b) tests at 100 °C and varied strain rates. c) Snapshots of the fracture samples right before crack propagation corresponding, from bottom to top, to the tests performed at  $\dot{\epsilon} = 0.017 \text{ s}^{-1}$ ,  $0.17 \text{ s}^{-1}$ , and  $1.7 \text{ s}^{-1}$ .

To explain this change in behavior when moving from tensile to fracture tests, we must consider the specific mechanisms that lead to failure in the two cases. In standard tensile tests, the stress/strain field is homogenous, and failure starts with crack nucleation somewhere in the material. The results in Figure 1-c and Figure 6-a indicate that nucleation is time-dependent, i.e., it occurs at lower strains for materials stretched at lower rates. Due to the transient nature of these networks [34], at lower rates the crosslinks are subjected to stress for longer times, promoting disassociation and loss of connectivity at strains lower than the ones of the samples stretched at higher rates.

In contrast, in fracture tests the initial stress-strain field is not homogenous due to the presence of the notch. Thus, delocalization is critical to prevent local failure at the crack tip and will matter more than the nominal strain reached in the bulk [6]. Indeed, from Figure 6-c the highly stretched, highly dissipating region around the notch extends to a larger area before propagation for the slowly stretched sample. Increasing the size of such a region has been connected to an increase in  $\Gamma$  for other soft, tough materials [2, 9, 11, 16].

The key insights from the fracture tests are:

- Continuously loaded fracture tests show a sharp transition from notch-resistant to notch-sensitive with increased T or  $\dot{\epsilon}$ . This is similar to the behavior observed in fatigue with increased T and applied strain.
- Fracture toughness,  $\Gamma$ , decreases with increasing T similar to the decrease observed for toughness,  $W$ , in tensile tests. However,  $\Gamma$  increases with decreasing  $\dot{\epsilon}$  which is *opposite* to what happens to  $W$ .
- Stress and strain delocalization is key to understanding the differences observed between fracture and tensile tests and is strongly rate-dependent for these TPEEs.

To quantify the extent of blunting and delocalization at the different testing conditions and Mw's, we next analyze the crack shape right before and during propagation as well as study how the strain fields evolve via DIC.

### Crack shape and propagation speed

To explain the high toughness of these materials, we need to estimate the volume involved in the process zone. Following the work of Scetta *et al.* [4] to quantify the difference in crack shape and estimate the size of the process zone [2] at the different testing conditions, we measure the radius of the crack tip right before ( $R$ ) and during crack propagation ( $R_{prop}$ ). The former is always larger than the latter as shown in the snapshot in Figure 4-c. The radius is calculated using a parabolic curve fit (yellow line in Figure 7-a).

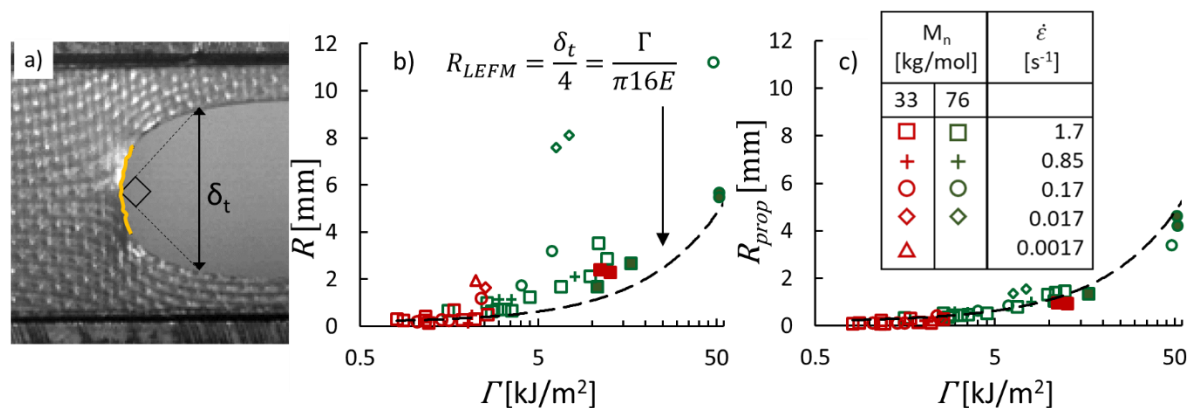


**Figure 7:** a) Example of parabolic fitting at the crack tip.  $\delta_t$  is the crack tip opening displacement [52]. b-c) Radius of the crack tip right before crack propagation,  $R$ , (b) and during propagation,  $R_{prop}$  (c) versus fracture toughness,  $\Gamma$ . The dashed line corresponds to the LEFM prediction for a hyperelastic material in plane stress calculated using the equation given, where  $E$  is the initial modulus [54]. Figure S4 shows zoomed in plots at low  $\Gamma$ . Data points where SIC of the SB is expected to occur are denoted with filled symbols. The data point of Mn=78 kg/mol at  $\dot{\epsilon}$  =0.0017 is missing as with our test setup, the sample is characterized by extreme blunting and either fails in a region different than the one where the notch was placed or slips from the grips before failure occurs

Figure 7 shows that  $R$  and  $R_{prop}$  plotted as a function of  $\Gamma$  for different testing conditions and Mw seemingly follow a single envelope. This implies the same  $\Gamma$  mechanism governs the failure of these materials at all the different testing conditions and Mw. The radii of the high-Mw sample seem to follow the same trend of the low-Mw one, but shifted to higher  $\Gamma$ , indicating that additional energy is required to nucleate cracks in the highly stretched region for the high-Mw sample.

The observed radii are compared with the linear elastic fracture mechanics (LEFM) prediction in plane stress for hyperelastic materials from Mac Donald *et al.* [54] (see supplemental information for more details on the derivation of the relationship between  $R_{LEFM}$  and  $\delta_t$ ).  $R$  starts to deviate from this prediction at  $\Gamma \sim 3 \text{ kJ/m}^2$ . The scattering in the  $R$  data is attributed to the stochastic initiation of cracks in the highly stretched region ahead of the notch [6, 54]. In contrast,  $R_{prop}$  is much less scattered and nicely follows the scaling as proposed by Mac Donald. This could be due to the high crack-propagation speeds, which translate into high deformation rates ahead of the crack tip, resulting in the material behaving more elastically than viscously at the propagating crack tip.

Until now we have focused on the initiation of failure – i.e. what conditions will cause a crack to begin to propagate. The fracture tests also allow us insight into how a crack moves during propagation. Recall from the introduction that the energy dissipated during loading is not available to drive crack growth and hence we focus on the critical energy for crack propagation,  $\Gamma_{local}$ , given by equation 1 when  $\varepsilon = \varepsilon_f$ ,  $G = \Gamma$  and  $g_{local} = \Gamma_{local}$ . Figure 8 plots  $\Gamma_{local}$  versus the observed crack propagation speed ( $v$ ). This is similar to what is typically done for tearing tests [2, 6, 7, 54] and steady-state crack-propagation tests [57-59], i.e., where the material is stretched to a given  $G$  or  $g_{local}$  and the crack velocity is measured while the crosshead displacement is kept fixed. We had to use continuous loading for our fracture tests rather than the latter approach due to the high stability of the crack tip below a critical displacement (Figure 3). However, since the measured crack propagation speed ( $\sim 300 \text{ mm/s}$ ) is significantly higher than the maximum adopted crosshead-displacement speed ( $\sim 8 \text{ mm/s}$ ) we believe a comparison can still be made.

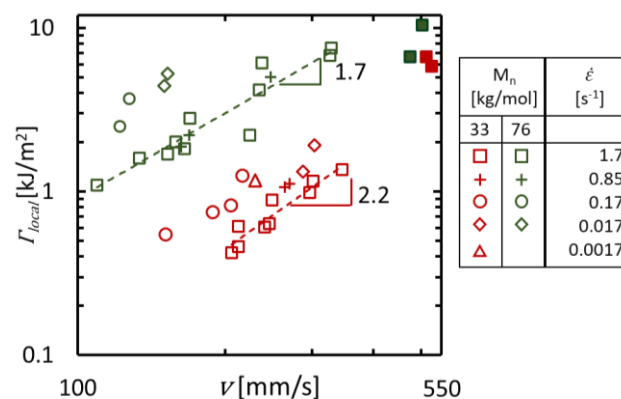


**Figure 8:** Critical energy for crack propagation,  $\Gamma_{local}$ , versus the crack propagation speed,  $v$ , at different testing conditions. The fitting with a power law is done only on the data at  $\dot{\varepsilon} = 1.7 \text{ s}^{-1}$  (squares) and  $T > RT$ . See table S1 for a summary of testing conditions. Data points where SIC of the SB is expected to occur are denoted with filled symbols.

For purely elastic materials,  $G$  is independent of  $v$  [2, 6, 7, 55] or shows a weak power-law dependence ( $G \sim v^n$ ) with the exponent  $n$  varying between 0.1 and 1 [2, 7, 57, 59-61]. For comparison, systems with modest dissipation such as physically associating triblock copolymer gels have  $n = 0.4$  [56] and for filled silicone elastomers  $n = 0.25-0.4$  [62]. These TPEEs show a strong power-law dependence of  $\Gamma_{local}$  (and thus  $g_{local}$ ) on the propagation velocity with  $n = 1.7$  or  $2.2$  for

low and high Mw, respectively. This indicates a highly viscous behavior for which a higher energy cost must be paid to propagate the crack at higher speeds. The rate dependence remains similar with increasing Mw, but the data are shifted to higher values of  $\Gamma_{local}$ . At lower  $\dot{\epsilon}$ 's, a higher  $\Gamma_{local}$  is required for the same crack velocity at the same  $v$  due to the higher energy required to initiate failure. Lower  $v$  generally corresponds to higher temperature (see Table S1).

To summarize, the crack shape is reasonably described by the LFM model for most of the tests we performed. However, locally in the zone of failure there is a strong rate dependent contribution.

Next we analyze the local strain fields via Digital Image Correlation (DIC) to understand if more delocalization occurs at the notch tip at lower loading rates and how it evolves with time.

#### **Digital Image Correlation (DIC) – rate effect on the local strain field**

The closest point to the crack tip we can resolve is at a distance of  $\sim 0.3$  mm; thus, we are unable to resolve the local strain field where failure or damage eventually initiate [6, 16]. However, we can compare the larger scale delocalization behavior by comparing the area where local strains are significantly higher than the bulk. Figure 9 shows the local strain fields near the notch tip for low-Mw fracture samples stretched at RT at strain rates between  $0.17$  and  $1.7$   $s^{-1}$  with nominal strain,  $\epsilon_N$ , of 25% and 38%. The highly-strained region considerably increases in area with decreased loading rate and increased strains.

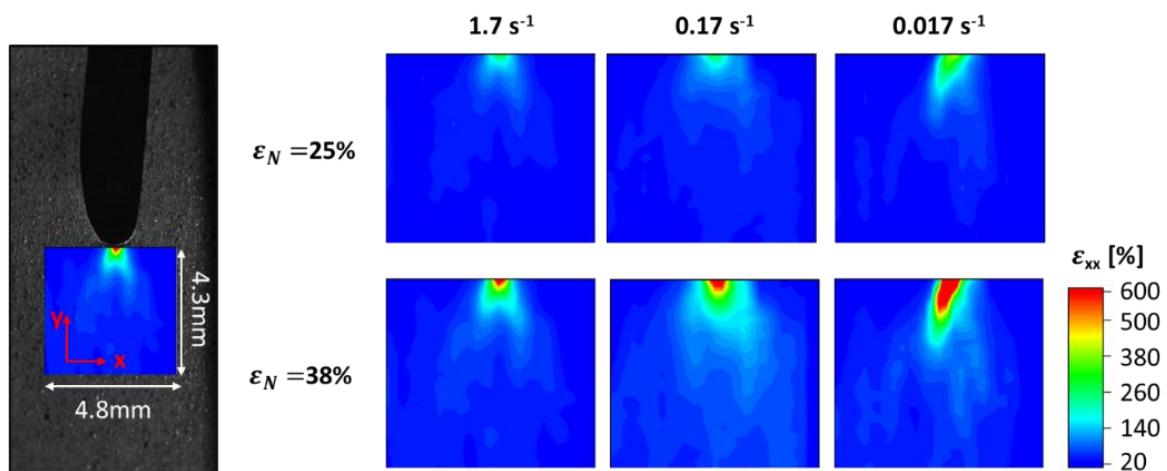


**Figure 9:** The left image shows the  $4.25 \times 4.80$   $mm^2$  area ahead of the crack tip analyzed via DIC. The stretching direction is denoted as x. The local strain fields for low-MW fracture samples tested at RT with nominal strains of 25% and 38% and strain rates between  $0.017$   $s^{-1}$  to  $1.7$   $s^{-1}$  are shown to the right.

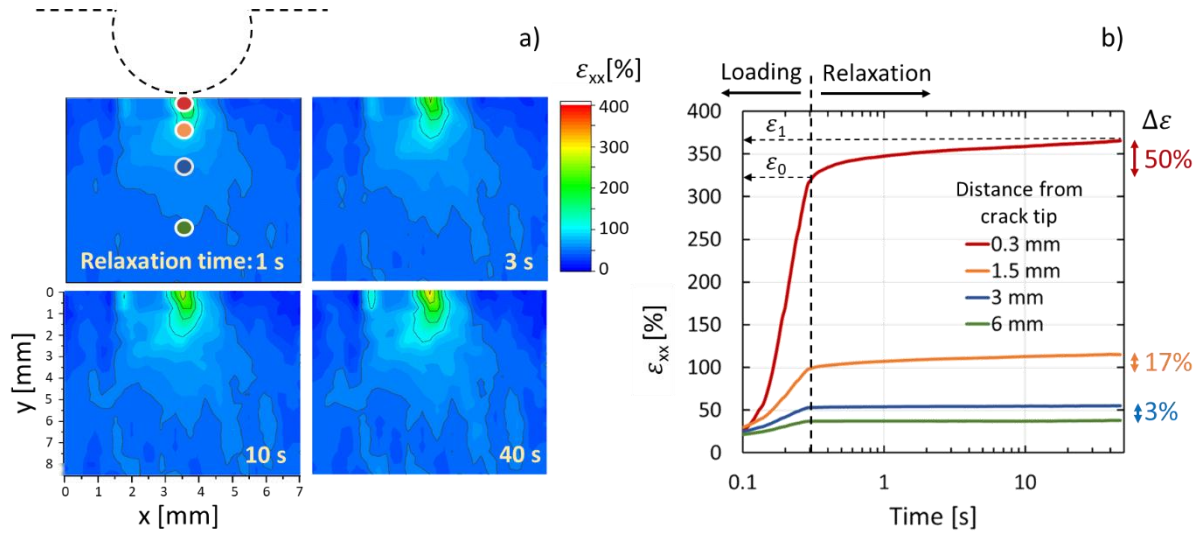


**Figure 10:** a) Local strain field in an  $8.5 \times 7\text{mm}^2$  area in front of the crack tip. b) Local strain field versus time at different distances from the crack tip, highlighted in (a) with the same color code. The increase in strain since stress relaxation started,  $\Delta\epsilon = \epsilon_1 - \epsilon_0$ , is noted at the right.

To further investigate the time-dependency of the delocalization process, we evaluate local strain evolution at the crack tip during stress relaxation. The test is performed on a low Mw-sample at RT with  $\epsilon_N = 40\%$  and the fastest loading rate ( $1.7\text{ s}^{-1}$ ) to minimize the amount of delocalization occurring during loading. Figure 10-a shows that even at constant  $\epsilon_N$  delocalization increases significantly with time. The increase in local strain with time at different distances from the crack tip is shown in Figure 10-b. After 40 s, the local strain increases by 50%  $\sim 0.3\text{ mm}$  from the crack tip and by lower amounts further away. The closer to the crack tip, the faster the local strain increases with time.

While we are not able to resolve strains very close to the crack tip where failure initiates ( $< 1\ \mu\text{m}$ ), the increase in strain with time at larger distances does point to delocalization of strain and hence lowering of the stresses at the crack tip. Note that this delocalization is more prominent at lower strain rates and hence we expect the driving stress for failure initiation and propagation to have reduced more under those boundary conditions. Thus, even though we observe an increase in strain, very near the crack tip, the sample is dissipating energy via redistribution and lowering the driving force for crack propagation. This is likely why standard steady-state fracture tests did not result in crack propagation for these samples and why continuous loading is necessary to observe failure.

The strain mapping by DIC shows that higher  $\Gamma$  is connected with larger process zones where high-strains and energy dissipation occur. A common way to estimate the length scale of the process zone is to calculate the elasto-adhesive length which equals  $\Gamma/E$  (see Table S1), where  $E$  is the elastic modulus of the material (values in Figure S5). For context, typical values of  $\Gamma/E$  are a few nanometers for hard, brittle silica glass, 0.01–0.1 mm for agar gels, 1–10 mm for DN gels and vulcanized rubber, and up to 100 mm for extremely tough and soft bilayer hybrid gels [6]. For these TPEEs,  $\Gamma/E$  ranges between 0.1 and 5.4 mm depending on the testing condition. It decreases with increasing T and  $\dot{\epsilon}$ . Note that when  $\Gamma/E$  approaches the sample's size (in this case, the initial height is 5 mm), the results may not be geometry independent [2]. We observe that when  $\Gamma/E > 1.5\text{ mm}$ , cracks propagate parallel to the stretching direction, likely due to extreme orientations reached to a large area ahead of the crack tip. The data falling in this regime were not considered in the

calculation of  $R_{prop}$ ,  $v$ , and for the following analysis. Fracture at these conditions may be measurable using larger samples.

In summary, DIC confirms that the delocalization process near the crack tip is strongly rate dependent with the highly strained area ahead of the crack tip significantly increasing with decreasing loading rate and with time at fixed displacement. Local strains exceed those of the bulk up to several mm from the crack tip. Transferring a significant amount of stress (or strain) from the crack tip to a neighboring volume involves crystal breakup and chain orientation [16, 19, 20, 34] which require time to occur. Viscoelastic processes controlling the strain-dependent microstructural evolution of TPEEs allow redistribution and accommodation of stress [5] and is linked to the strong temperature and rate dependent notch-sensitivity for TPEEs.

## Discussion

Now that we have described the observations on the deformation, fatigue, and fracture behavior of these TPEEs, we aim to place these observations in the wider context of soft, tough materials in terms of process zone size and key mechanical features governing their behavior. Similar to DN gels, TPEEs undergo significant damage and dissipation during loading. The resulting microstructure is characterized by more elasticity (Figure 2) and a much lower modulus [5, 20, Table S2] than the initial one. Given these similarities in the mechanical behavior, we compare our observations with models developed by Brown [11] and Tanaka [8,9] to explain the toughness of DN gels.

### Comparison of TPEE toughness with predictions from micromechanical models

The idea that the high toughness of soft materials originates from the formation of a large plastically deformed volume ahead of the crack tip where dissipation occurs originates with the Dugdale zone model. It was first developed for hard elasto-plastic materials, i.e., showing minimal or zero strain hardening [63]. In this model, the stress is uniform and equal to the yield stress ( $\sigma_y$ ) throughout the process zone. Brown [11] extended the model to the case of glassy systems characterized by crazing and then to DN gels [8, 9, 11]. Tanaka extended the approach to consider DN gels with strain hardening [9].

This approach relies on the concept that the crack only propagates when the elastic energy per unit volume ( $W_{2nd}$ ) stored in the damaged second network times the thickness of the yielded zone ( $H_0$ ) exceeds the fracture energy of the second network ( $G_2$ ). Thus,

$$G_2 = H_0 W_{2nd} \quad (6)$$

The macroscopic fracture energy,  $\Gamma$ , is given by the area below the loading curve ( $\sim \sigma_y \varepsilon_f$ ) times  $H_0$ ,

$$\Gamma = H_0 \sigma_y \varepsilon_f \quad (7)$$

where  $\varepsilon_f$  is the final extensibility of the yielded material.

The difference between Brown's and Tanaka's approach is in the assumptions on the shape of the stress-strain curve, and hence, on how  $W_{2nd}$  and  $H_0$  are defined. The mechanical behavior assumed for each model is compared with the typical response for a TPEE in Figure 11-a.

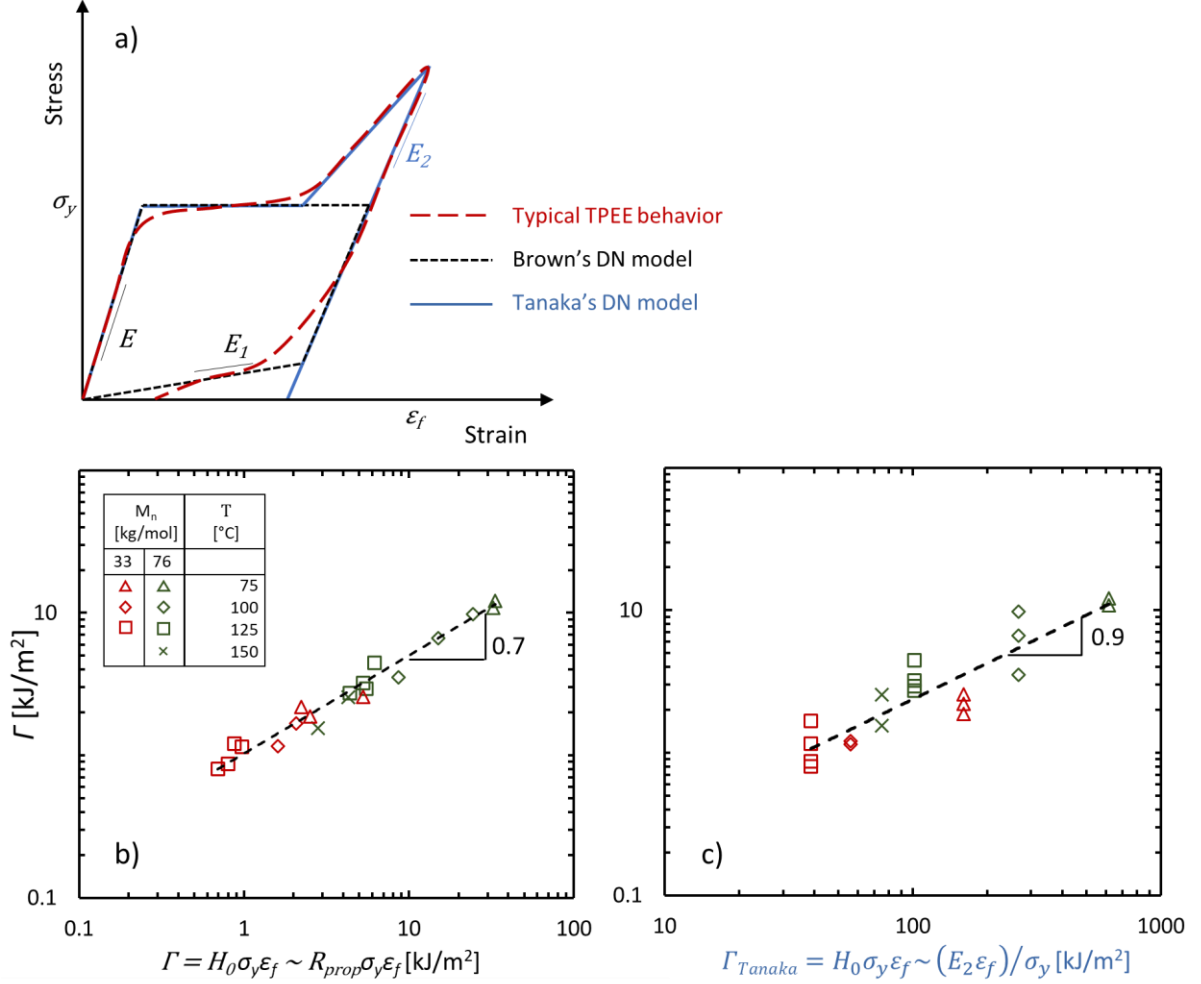


**Figure 11:** a) Schematic deformation behavior for the assumptions in Brown's and Tanaka's DN model as well as what is typical for a TPEE. The corresponding expressions for the fracture toughness are included. Below the measured fracture toughness,  $\Gamma$ , measured for low- and high-MW samples at  $\dot{\epsilon} = 1.7 \text{ s}^{-1}$  and varied temperatures is compared with that predicted either using our assumption (b) or Tanaka's model (c). For the former, we assume the undeformed damage zone thickness  $H_0$  is equal to the observed  $R_{prop}$ . For the Tanaka's model, we assume  $G_2$  is a constant. Yield stress ( $\sigma_y$ ) and failure strain ( $\epsilon_f$ ) from corresponding standard tensile tests are used. Data collected at RT are omitted due to the presence of SIC of SBs.

In his model, Brown assumes constant stress after yielding of the 1<sup>st</sup> network and no strain hardening. The area under the unloading curve equals  $W_{2nd} \sim E_1 \epsilon_f^2$  where  $E_1$  is the low strain unloading modulus. Substituting into equations 6 and 7 results in  $G_2 \sim H_0 E_1 \epsilon_f^2$  and

$$\Gamma_{Brown} = H_0 \sigma_y \epsilon_f = \frac{G_2 \sigma_y}{E_1 \epsilon_f} \quad (8)$$

Note that in this case  $H_0$  is the thickness of the yielded zone after unloading.

Tanaka expanded on Brown's approach by considering the influence of strain hardening instead of only the yield stress, low strain modulus and failure strain. Considering the strain hardening, he estimates  $W_{2nd} \sim \sigma_y^2 / E_2$  where  $E_2$  is the unloading modulus at high strain. The yielded zone size can be estimated by  $H_0 \sim G_2 / W_{2nd} \sim G_2 E_2 / \sigma_y^2$ . Note in Tanaka's treatment  $H_0$  is

the deformed size of the damage zone, rather than the unloaded size as Brown uses. Substituting gives the estimate of fracture toughness from Tanaka's approach

$$\Gamma_{Tanaka} = H_0 \sigma_y \varepsilon_f = \frac{G_2 E_2 \varepsilon_f}{\sigma_y} \quad (9)$$

To assess whether our data follows the trends predicted by either approach, we use  $\sigma_y$  and  $\varepsilon_f$  measured from tensile tests (Table S2). Due to the lack of tensile tests at all  $\dot{\varepsilon}$ 's for all temperatures, we use values determined at  $\dot{\varepsilon} = 1.7 \text{ s}^{-1}$ . The high and low strain unloading moduli,  $E_1$  and  $E_2$ , are determined from cyclic tensile tests at the highest applied strain we were able to measure at each condition (values in Table S3). As we lack a method to determine  $G_2$  for our materials, we treat it as a constant. If chain scission occurs during crack propagation and the yielded network is fully elastic,  $G_2$  depends on the bond strength of the covalent bonds along the chain which is independent of temperature. In this case, our assumption might not be too far from reality. For TPEEs,  $\sigma_y$  corresponds to the stress at which the major break-up of the HB crystals occurs, which is related to the main source of energy dissipation in TPEEs [4, 5, 16, 20] rather than the breaking of covalent bonds as in DN gels.

The main difficulty in comparing our observed toughness with these micromechanical models is how to estimate the size of the yielded zone,  $H_0$ . The observed crack tip radius is influenced by the process zone size [2]. Thus, we use  $R_{prop}$  as a measure for  $H_0$ . Because  $R_{prop}$  is measured while the elastic part of the input energy is being released, we believe it gives a better description for the unloaded size of the yielded zone than the radius prior to propagation which reflects the state of the process zone during deformation, i.e., including the elastic fraction that would be recovered upon unloading. While assuming  $R_{prop}$  and  $H_0$  should be related, we acknowledge that there is no proof of direct proportionality. The assumption of  $R_{prop} \sim H_0$  leads to a reasonably good agreement between the measured fracture toughness and the prediction following the general Brown's and Tanaka's approach, as shown in Figure 11-b. The data collapse across the various testing conditions and Mw, following a single trend with  $\Gamma \sim (R_{prop} \sigma_y \varepsilon_f)^{0.7}$ .

However, a perfect agreement with the model would entail a power-law exponent of 1 and the deviation from this power-law exponent of 1 suggests this approach does not capture all the key variables. The irreversible work per unit volume estimated as  $\sigma_y \varepsilon_f$  underestimates that of our materials, where additional fragmentation of the HB crystals, and hence dissipation occurs beyond  $\sigma_y$ . That is to say, we have neglected the contribution from strain hardening.

If instead of  $R_{prop}$  as a measure for the yielded size, we use  $H_0$  estimated according to Tanaka's model, we see that the power-law exponent is increased to 0.9 (Figure 11-c), showing a good agreement our Tanaka's model with our data. This implies that the high-strain properties significantly contribute to the observed toughness of TPEEs similar to DN gels where a substantial increase in toughness was observed for those showing strain hardening [9]. The combination of a yielding mechanism and strain hardening leads to the development of a large and stable, yielded zone around the crack tip and to high  $\Gamma$ . Tanaka's model is also consistent with the requirement that a critical stress state is reached at the crack tip to extend the crack surface. Indeed, they show that assuming linear elasticity and that the local stress shows an asymptotic behavior, leads to  $\sigma(x) \approx \sigma_y \sqrt{h/x}$ , where  $x$  is the distance from the crack tip to the bulk, further leading to  $h \propto 1/\sigma_y^2$ , in agreement with their model.

The fact that  $\Gamma$  is well described by the high-strain properties is consistent with the highly nonlinear mechanical response of our TPEEs and with the differences we see when varying Mw in

both fracture and tensile tests. The high-Mw samples have low-strain properties ( $\sigma_y$ ,  $E_1$ ) similar to the low-Mw ones. However, large differences are seen at high-strains, i.e.,  $\varepsilon_f$ ,  $\sigma_f$  and  $E_2$  increase with increasing Mw.

The agreement between the observed TPE toughness and that predicted by the DN gel models suggests that the high toughness of TPE's originates from the large volume to which the stresses and strains at the crack tip are delocalized and that the yield stress, the final extensibility, and the strain reinforcement ( $E_2$ ) of the material play an important role in determining the extent of delocalization.

### Rate-dependency of delocalization and its role on the fracture resistance of TPEs

Despite the reasonable scaling between measured toughness of these TPEs and key variables predicted by the elastic DN models, these models fail to capture the significant increase of  $\Gamma$  when  $\dot{\varepsilon}$  decreases. In fact, the models would predict the opposite since  $\sigma_f$ ,  $\sigma_y$ , and  $\varepsilon_f$  decrease with decreasing  $\dot{\varepsilon}$ . DIC data (Figure 9 and 10) clearly show that the delocalization mechanism is strongly time dependent, i.e., the size of the yielded or damaged zone strongly depends on the loading rate. From the relaxation curves in Figure 10-b, we estimate the rate of strain evolution ( $\partial\varepsilon_{xx}/\partial t$ ) at different distances from the crack tip (Figure S6). This relates to the time scales of the viscoelastic processes responsible for transferring damage to a larger region around the crack tip. The rate of strain evolution is estimated as  $\sim 0.01 \text{ s}^{-1}$  near the crack tip, which is in the same order of the nominal  $\dot{\varepsilon}$  of our tests. This could explain why at some temperatures increasing  $\dot{\varepsilon}$  by just one order of magnitude can change the behavior of the material from notch-resistant to notch-sensitive despite less dramatic changes observed in standard tensile tests with similar changes in rate.

We propose that the rate dependence can be understood by considering the time required to sufficiently delocalize the damage zone compared with the time required to nucleate a critical crack at the notch tip. The idea is schematically depicted in Figure 12. Treating delocalization as a viscoelastic process we can define a characteristic time,  $\tau_{deloc}$ , which is the time needed to homogenize the high stress of a nanometric volume at the crack tip over a significant neighboring volume such that local failure is prevented. Analogously, we can define a local-failure time,  $\tau_{failure}$ , as the time required to nucleate a crack in the highly stretched region. Naturally, both characteristic times are T-, stress-, and Mw-dependent.

Stretching the notched sample to  $\varepsilon_{N,0}$  at  $t_0$  generates a strain gradient from the crack tip to the bulk. Whether the sample fails or not when further stretched to  $\varepsilon_N$  depends on the balance between  $\tau_{deloc}$ ,  $\tau_{failure}$ , and  $\dot{\varepsilon}$ . Simply, if the applied  $\dot{\varepsilon}$  is small enough to allow for delocalization to occur ( $\tau_{deloc} < 1/\dot{\varepsilon}$ ) and if the latter occurs before local failure does ( $\tau_{deloc} < \tau_{failure}$ ), the stresses redistribute to a larger volume and the material is notch-resistant. This involves the microstructure significantly rearranging dissipating more energy while relaxing stress locally at the crack tip and increasing blunting. Alternatively, if  $\dot{\varepsilon}$  is too high to allow for sufficient delocalization ( $\tau_{deloc} > 1/\dot{\varepsilon}$ ), or if the local failure occurs before delocalization ( $\tau_{deloc} > \tau_{failure}$ ), a crack initiates in the highly stretched region and rapidly propagates through the sample with little or no blunting visible at the crack tip. In this case, we observe a notch-sensitive response.

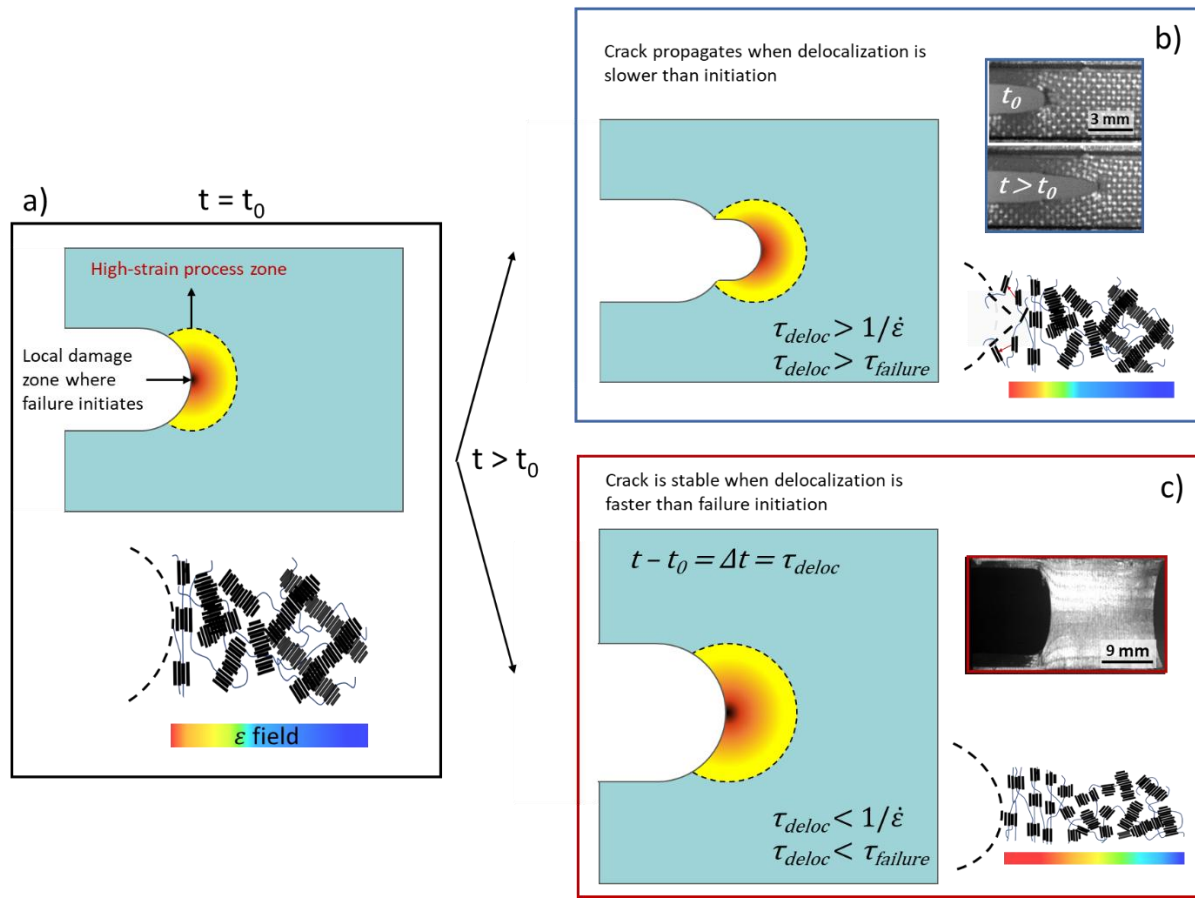


**Figure 12:** a) Cartoon representing the strain gradient that develops at the crack tip and the related change in morphology. Whether a crack propagates (b) or blunts (c) depends on the balance between the delocalization time ( $\tau_{deloc}$ ) required to expand the process zone, the time required to initiate failure ( $\tau_{failure}$ ) and the applied strain rate ( $\dot{\epsilon}$ ). The material will behave as notch-resistant when deformation is delocalized over a larger volume or as notch-sensitive when a crack initiates in the highly-stretched region before delocalization occurs.

## Conclusions

For the first time the failure behavior in tensile, fracture, and fatigue of an industrially relevant multiblock copoly(ether-ester) TPEE has been systematically evaluated. The key observations and insights are:

- A sharp transition from notch-resistant to notch-sensitive occurs with small changes in the applied deformation rates or temperature both in fatigue and continuously loaded fracture tests. Surprisingly, there appears to be a threshold strain below which the cracks do not propagate in fatigue. If the maximum strain exceeds the threshold strain the sample fails in just one cycle.
- While decreasing strain rate increases toughness when the stress field is homogeneous as in tensile tests, it decreases toughness when notches lead to inhomogeneous stress fields as in fracture tests.

- The failure behavior is governed by a single mechanism at all temperatures above the SIC range and deformation-rate ranges tested. The crack shape is reasonably described by the LEFM model. However, locally in the zone of failure there is strong viscous contribution as indicated by the very high-rate dependency observed ( $\Gamma_{local} \sim V^{-2}$ ). Thus, a higher energy cost must be paid to propagate the crack at higher speeds.
- Stress and strain delocalization is key to achieve high toughness and notch resistance. DIC confirms delocalization near the crack tip is strongly rate dependent and local strains exceed those of the bulk up to several mm from the crack tip. Viscoelastic processes controlling the strain-dependent microstructural evolution of TPEEs allow redistribution and accommodation of stress.
- The high-strain properties (yield stress, failure strain, and strain-hardening) have a dominant contribution to toughness because they influence the size of the process zone over which delocalization occurs. Micromechanical models developed for DN gels generally do a good job describing TPEE toughness; however, being time-independent elastic models they fail to capture the increase in toughness with decreases strain rate.
- We rationalize the rate dependent toughness by considering whether the time required to nucleate a crack in the highly strained region near the crack tip is shorter than the time needed to transfer the stress from this region to a sufficient neighboring volume to prevent local failure.

This work highlights the challenges in describing failure for systems with highly strain dependent morphologies that exhibit a distinct temperature and rate dependence. While this presents a scientific challenge, it also presents itself as a challenge for this class of materials to be adopted further as sustainable alternatives in demanding applications where they intend to replace the more established chemically crosslinked systems. Knowledge of the exact failure mechanism and hence the interplay of local stress state versus material response should allow us to harness this behavior as it also manifests in extremely useful ways such as the high resistance to fatigue crack propagation under many conditions. Experimental methods to more rapidly assess the regions of notch-resistance and modeling approaches to couple those results with relevant application conditions are necessary if accurate lifetime predictions for TPEs are to be realized.

## Acknowledgement

This work was financially supported by funding from the H2020 Program (MARIE SKŁODOWSKA-CURIE ACTIONS) of the European Commission's Innovative Training Networks (H2020-MSCA-ITN-2017) under DoDyNet REA Grant Agreement N°0.765811. The authors thankfully acknowledge Ron Riedel for the help with setting up the high-speed camera.

## References

- 1) Fakirov, S., Handbook of condensation thermoplastic elastomers (Wiley-VCH, Weinheim, 2005).
- 2) Creton, C., & Ciccotti, M. (2016). Fracture and adhesion of soft materials: a review. *Reports on Progress in Physics*, 79(4), 046601.
- 3) Sanoja, G. E., Morelle, X. P., Comtet, J., Yeh, C. J., Ciccotti, M., & Creton, C. (2021). Why is mechanical fatigue different from toughness in elastomers? The role of damage by polymer chain scission. *Science advances*, 7(42), eabg9410.
- 4) Scetta, G., Selles, N., Heuillet, P., Ciccotti, M., & Creton, C. (2021). Cyclic fatigue failure of TPU using a crack propagation approach. *Polymer Testing*, 97, 107140.
- 5) Scetta, G., Euchler, E., Ju, J., Selles, N., Heuillet, P., Ciccotti, M., & Creton, C. (2021). Self-Organization at the Crack Tip of Fatigue-Resistant Thermoplastic Polyurethane Elastomers. *Macromolecules*, 54(18), 8726-8737.

- 6) Long, R., Hui, C. Y., Gong, J. P., & Bouchbinder, E. (2021). The fracture of highly deformable soft materials: A tale of two length scales. *Annual Review of Condensed Matter Physics*, 12, 71-94.
- 7) Tanaka, Y., Kuwabara, R., Na, Y. H., Kurokawa, T., Gong, J. P., & Osada, Y. (2005). Determination of fracture energy of high strength double network hydrogels. *The Journal of Physical Chemistry B*, 109(23), 11559-11562.
- 8) Tanaka, Y. (2007). A local damage model for anomalous high toughness of double-network gels. *EPL (Europhysics Letters)*, 78(5), 56005.
- 9) Tanaka, Y., Kawauchi, Y., Kurokawa, T., Furukawa, H., Okajima, T., & Gong, J. P. (2008). Localized Yielding Around Crack Tips of Double-Network Gels. *Macromolecular rapid communications*, 29(18), 1514-1520.
- 10) Gong, J. P., Katsuyama, Y., Kurokawa, T., & Osada, Y. (2003). Double-network hydrogels with extremely high mechanical strength. *Advanced materials*, 15(14), 1155-1158.
- 11) Brown, H. R. (2007). A model of the fracture of double network gels. *Macromolecules*, 40(10), 3815-3818.
- 12) Lin, S., Liu, X., Liu, J., Yuk, H., Loh, H. C., Parada, G. A., ... & Zhao, X. (2019). Anti-fatigue-fracture hydrogels. *Science advances*, 5(1), eaau8528.
- 13) Mullins, L. (1948). Effect of stretching on the properties of rubber. *Rubber chemistry and technology*, 21(2), 281-300.
- 14) Zhang, W., Liu, X., Wang, J., Tang, J., Hu, J., Lu, T., & Suo, Z. (2018). Fatigue of double-network hydrogels. *Engineering Fracture Mechanics*, 187, 74-93.
- 15) Bai, R., Yang, J., & Suo, Z. (2019). Fatigue of hydrogels. *European Journal of Mechanics-A/Solids*, 74, 337-370.
- 16) Mzabi, S., Berghezan, D., Roux, S., Hild, F., & Creton, C. (2011). A critical local energy release rate criterion for fatigue fracture of elastomers. *Journal of Polymer Science Part B: Polymer Physics*, 49(21), 1518-1524.
- 17) Mayumi, K., Guo, J., Narita, T., Hui, C. Y., & Creton, C. (2016). Fracture of dual crosslink gels with permanent and transient crosslinks. *Extreme Mechanics Letters*, 6, 52-59.
- 18) Gaymans, R. J., "Segmented copolymers with monodisperse crystallizable hard segments: Novel semi-crystalline materials," *Prog. Polym. Sci.* 36, 713-748 (2011).
- 19) Konyukhova, E. V., V. M. Neverov, Y. K. Godovsky, S. N. Chvalun, M. Soliman, "Deformation of Polyether-Polyester Thermoelastoplastics: Mechano-thermal and Structural Characterisation," *Macromol. Mater. Eng.* 287, 250-265 (2002).
- 20) Sbrescia, S., J. Ju, T. Engels, E. Van Ruymbeke, M. Seitz, "Morphological origins of temperature and rate dependent mechanical properties of model soft thermoplastic elastomers," *J. Polym. Sci.* 59, 477-493, (2021).
- 21) Van Bogart, J. C., Lilaonitkul, A. M. N. U. E. Y., Lerner, L. E., & Cooper, S. L. (1980). Morphology and properties of short segment block copolymers. *Journal of Macromolecular Science, Part B: Physics*, 17(2), 267-301.
- 22) Deschamps, A. A., Grijpma, D. W., & Feijen, J. (2001). Poly (ethylene oxide)/poly (butylene terephthalate) segmented block copolymers: the effect of copolymer composition on physical properties and degradation behavior. *Polymer*, 42(23), 9335-9345.
- 23) Dahrouch, M., Schmidt, A., Leemans, L., Linssen, H., & Goetz, H. (2003, October). Synthesis and properties of poly (butylene terephthalate)-poly (ethylene oxide)-poly (dimethylsiloxane) block copolymers. In *Macromolecular Symposia* (Vol. 199, No. 1, pp. 147-162). Weinheim: WILEY-VCH Verlag.

- 24) Sup Lee, H., Ra Yoo, S., & Won Seo, S. (1999). Domain and segmental deformation behavior of thermoplastic elastomers using synchrotron SAXS and FTIR methods. *Journal of Polymer Science Part B: Polymer Physics*, 37(22), 3233-3245.
- 25) Biemond, G. J. E., Feijen, J., & Gaymans, R. J. (2008). Tensile properties of segmented block copolymers with monodisperse hard segments. *Journal of materials science*, 43(10), 3689-3696..
- 26) Nébouy, M., Louhichi, A., & Baeza, G. P. (2020). Volume fraction and width of ribbon-like crystallites control the rubbery modulus of segmented block copolymers. *Journal of Polymer Engineering*, 40(9), 715-726.
- 27) Stribeck, N., Sapoundjieva, D., Denchev, Z., Apostolov, A. A., Zachmann, H. G., Stamm, M., & Fakirov, S. (1997). Deformation behavior of poly (ether ester) copolymer as revealed by small-and wide-angle scattering of X-ray radiation from synchrotron. *Macromolecules*, 30(5), 1329-1339.
- 28) Stribeck, N., Fakirov, S., Apostolov, A. A., Denchev, Z., & Gehrke, R. (2003). Deformation Behavior of PET, PBT and PBT-Based Thermoplastic Elastomers as Revealed by SAXS from Synchrotron. *Macromolecular Chemistry and Physics*, 204(7), 1000-1013.
- 29) Unsal, E., Yalcin, B., Yilgor, I., Yilgor, E., & Cakmak, M. (2009). Real time mechano-optical study on deformation behavior of PTMO/CHDI-based polyetherurethanes under uniaxial extension. *Polymer*, 50(19), 4644-4655.
- 30) Nogales, A., Sics, I., Ezquerra, T. A., Denchev, Z., Balta Calleja, F. J., & Hsiao, B. S. (2003). In-situ simultaneous small-and wide-angle X-ray scattering study of poly (ether ester) during cold drawing. *Macromolecules*, 36(13), 4827-4832.
- 31) Yeh, F., Hsiao, B. S., Sauer, B. B., Michel, S., & Siesler, H. W. (2003). In-situ studies of structure development during deformation of a segmented poly (urethane- urea) elastomer. *Macromolecules*, 36(6), 1940-1954.
- 32) Niesten, M. C. E. J., & Gaymans, R. J. (2001). Tensile and elastic properties of segmented copolyetheresteramides with uniform aramid units. *Polymer*, 42(14), 6199-6207.
- 33) Zhu, P., Dong, X., & Wang, D. (2017). Strain-induced crystallization of segmented copolymers: deviation from the classic deformation mechanism. *Macromolecules*, 50(10), 3911-3921.
- 34) Aime, S., Eisenmenger, N. D., & Engels, T. A. P. (2017). A model for failure in thermoplastic elastomers based on Eyring kinetics and network connectivity. *Journal of Rheology*, 61(6), 1329-1342.
- 35) Sbrescia, S., Nicoletta, P., Engels, T., & Seitz, M. (2022). Effect of block length on the network connectivity and temperature resistance of model, soft thermoplastic elastomers. *Journal of Rheology*, 66(1), 177-185.
- 36) Sbrescia, S., Engels, T., E. Van Ruymbeke, M. Seitz, Molecular weight effects on the stress-relaxation behavior of soft thermoplastic elastomer by means of temperature scanning stress relaxation (TSSR). *Journal of Rheology*, under review.
- 37) Auriemma, F., C. De Rosa, M. Scoti, R. Di Girolamo, A. Malafronte, M. Christian D'Alterio, L. Boggioni, S. Losio, A. Caterina Boccia, and I. Tritto, "Structure and mechanical properties of ethylene/1-octene multiblock copolymers from chain shuttling technology," *Macromolecules* 52, 2669–2680 (2019).
- 38) Smith, T. L., "Tensile strength of polyurethane and other elastomeric block copolymers," *J. Polym. Sci. Part B Polym. Phys.* 12, 1825-1848 (1974).
- 39) Xie, H., H.Lu, Z. Zhang, X. Li, X. Yang, Y. Tu, "Effect of Block Number and Weight Fraction on the Structure and Properties of Poly(butylene terephthalate)-block-Poly(tetramethylene oxide) Multiblock Copolymers," *Macromolecules* 54, 2703-2710 (2021).
- 40) Zhang, T., Lin, S., Yuk, H., & Zhao, X. (2015). Predicting fracture energies and crack-tip fields of soft tough materials. *Extreme Mechanics Letters*, 4, 1-8.

- 41) Sun, J. Y., Zhao, X., Illeperuma, W. R., Chaudhuri, O., Oh, K. H., Mooney, D. J., ... & Suo, Z. (2012). Highly stretchable and tough hydrogels. *Nature*, 489(7414), 133-136.
- 42) Brown, H. R. (1991). A molecular interpretation of the toughness of glassy polymers. *Macromolecules*, 24(10), 2752-2756.
- 43) Gabriëlse, W., M. Soliman, K. Dijkstra, "Microstructure and phase behavior of block copoly (ether ester) thermoplastic elastomers," *Macromolecules* 34, 1685-1693 (2001).
- 44) Rivlin, R. S.; Thomas, A. G. Rupture of Rubber. I. Characteristic Energy for Tearing. *J. Polym. Sci.* 1953, 10, 291-318.
- 45) D. André, pydic, <https://gitlab.com/damien.andre/pydic> (2018).
- 46) Schmidt, A., Veeman, W. S., Litvinov, V. M., & Gabriëlse, W. (1998). NMR investigations of in-situ stretched block copolymers of poly (butylene terephthalate) and poly (tetramethylene oxide). *Macromolecules*, 31(5), 1652-1660.
- 47) Nébouy, M., Louhichi, A., & Baeza, G. P. (2020). Volume fraction and width of ribbon-like crystallites control the rubbery modulus of segmented block copolymers. *Journal of Polymer Engineering*, 40(9), 715-726.
- 48) Bhowmick, A. K. Threshold Fracture of Elastomers. *J. Macromol. Sci., Polym. Rev.* 1988, 28, 339-370.
- 49) Lake, G. J.; Lindley, P. B. Mechanical Fatigue Limit for Rubber. *Rubber Chem. Technol.* 1966, 39, 348-364.
- 50) Scetta, G. (2020). Fatigue cracking of thermoplastic elastomers (Doctoral dissertation, Université Paris sciences et lettres).
- 51) De, D. and Gent, A.N. (1996), Tear strength of carbon-black-filled compounds. *Rubber Chemistry and Technology*, 69(5), 834-850.
- 52) Krishnan, V. R., Hui, C. Y., & Long, R. (2008). Finite strain crack tip fields in soft incompressible elastic solids. *Langmuir*, 24(24), 14245-14253.
- 53) Lake, G. J.; Lindley, P. B. Cut Growth and Fatigue of Rubbers. *J. Appl. Polym. Sci.* 1964, 455, 292-300.
- 54) Mac Donald, K. A., & Ravichandran, G. (2020). Crack propagation and renucleation in soft brittle hydrogels. *International Journal of Fracture*, 222(1), 37-52.
- 55) Greensmith, H. W., Mullins, L., & Thomas, A. G. (1960). Rupture of rubber. *Transactions of the Society of Rheology*, 4(1), 179-189.
- 56) Seitz, M. E., Martina, D., Baumberger, T., Krishnan, V. R., Hui, C. Y., & Shull, K. R. (2009). Fracture and large strain behavior of self-assembled triblock copolymer gels. *Soft Matter*, 5(2), 447-456.
- 57) Baumberger, T., Caroli, C., & Martina, D. (2006). Fracture of a biopolymer gel as a viscoplastic disentanglement process. *The European Physical Journal E*, 21(1), 81-89.
- 58) Baumberger, T., Caroli, C., & Martina, D. (2006). Solvent control of crack dynamics in a reversible hydrogel. *Nature materials*, 5(7), 552-555.
- 59) Gent A N, Lai S M, Nah C and Wang C 1994 Viscoelastic effects in cutting and tearing rubber *Rubber Chem. Technol.* 67 610-8.
- 60) Y, Kuwabara R, Na Y H, Kurokawa T, Gong J P and Osada Y 2005 Determination of fracture energy of high strength double network hydrogels *J. Phys. Chem. B* 109 11559-62.
- 61) Cristiano A, Marcellan A, Keestra B J, Steeman P and Creton C 2011 Fracture of model polyurethane elastomeric networks *J. Polym. Sci. B* 49 355-67.
- 62) Yeh, C. J., Dowland, M., Schmidt, R. G., & Shull, K. R. (2016). Fracture and thermal aging of resin-filled silicone elastomers. *Journal of Polymer Science Part B: Polymer Physics*, 54(2), 263-273.
- 63) Dugdale, D. S. (1960). Yielding of steel sheets containing slits. *Journal of the Mechanics and Physics of Solids*, 8(2), 100-104.



## Supplemental Information

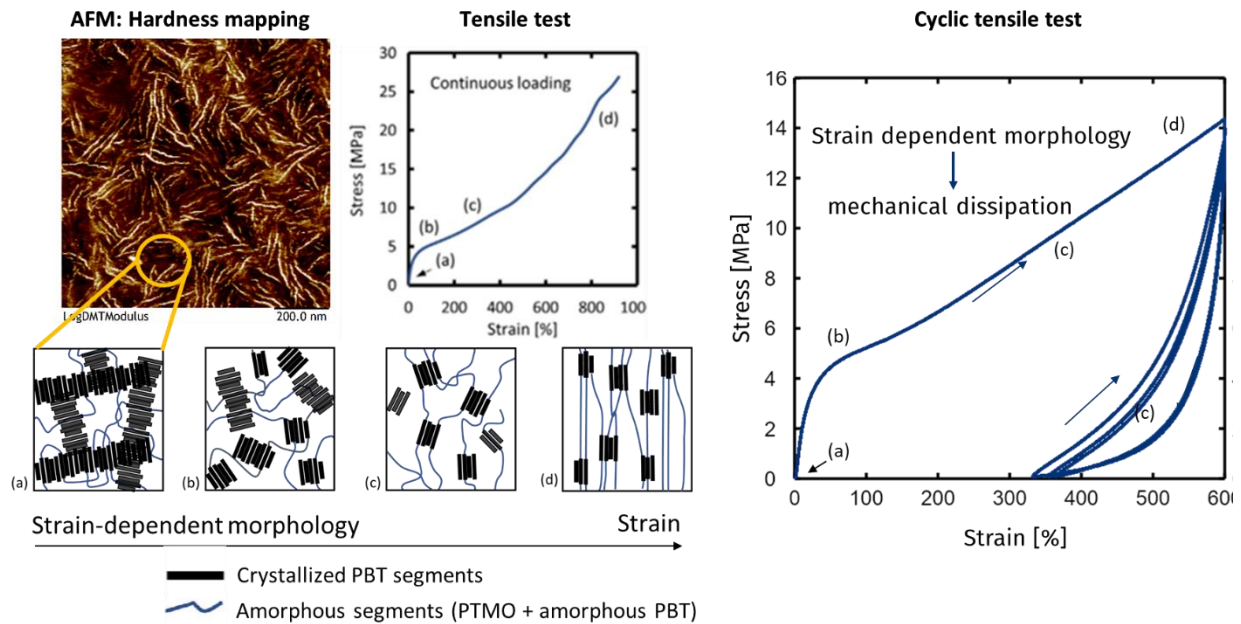
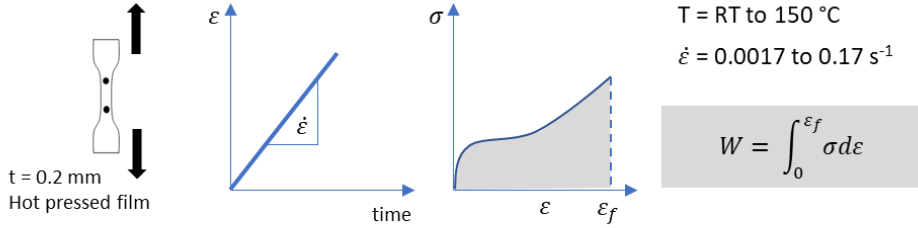
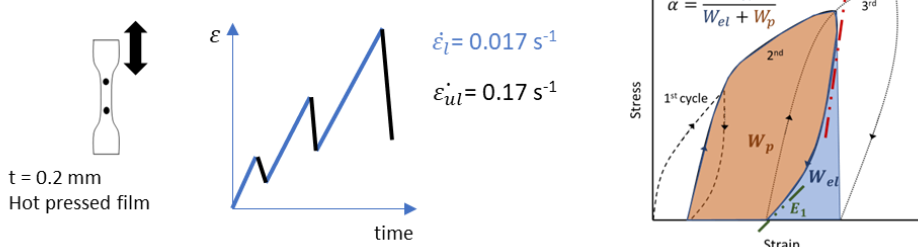


**Figure S1:** Description of the microstructure of the copoly(ether-ester) TPEs under study, including the changes it undergoes as the material is stretched. On the top-left, an AFM hardness mapping of the surface of one tested sample shows the high aspect ratio of the PBT crystals forming an interlocked hard phase. Details on the method for the AFM can be found in our previous study [20]. On the top-center, a stress-strain plot performed at RT on the low-Mw sample. Here, the different stages in strain where the microstructure is expected to change are highlighted. The corresponding changes are depicted on the bottom-left of the figure. On the right, a cyclic tensile test where the multiple cycles following the first one is done at the same level of strain. This last part substantiates the irreversible changes occurring to the microstructure, where the first cycle shows large hysteresis and plasticity, while the subsequent cycles exhibit considerably more elastic behavior, which remains relatively constant as the number of stretching cycles increases. Figure is rearranged from figures in our previous study [20].

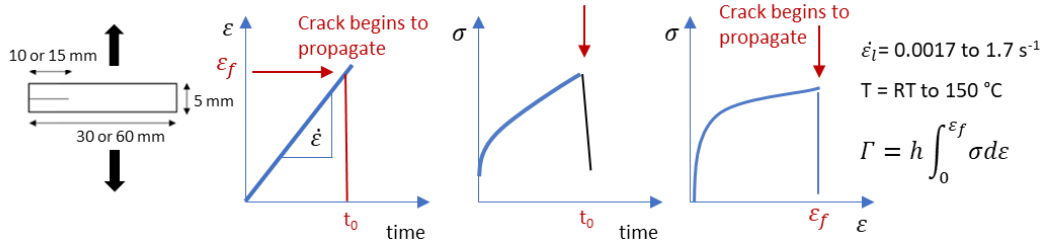
**Standard tensile tests**



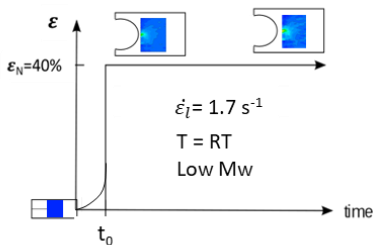
**Cyclic tensile tests**



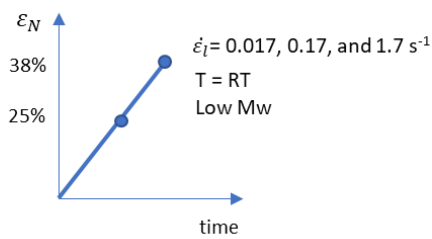
**Continuously loaded fracture tests**



**Stress relaxation of notched fracture specimen for DIC**



**DIC for fracture specimen loaded to fixed strain**



**Fatigue test protocol for lowMw samples**

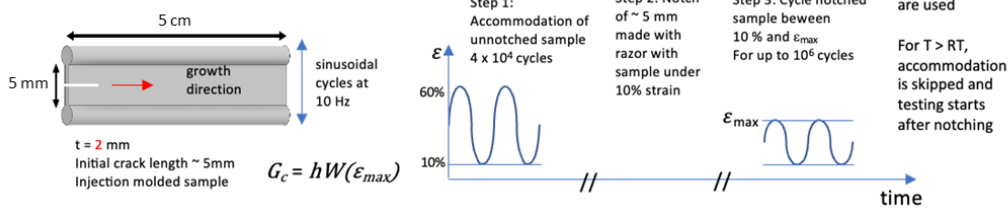


**Figure S2:** General overview of the testing methods, samples geometries and definitions of the variables.

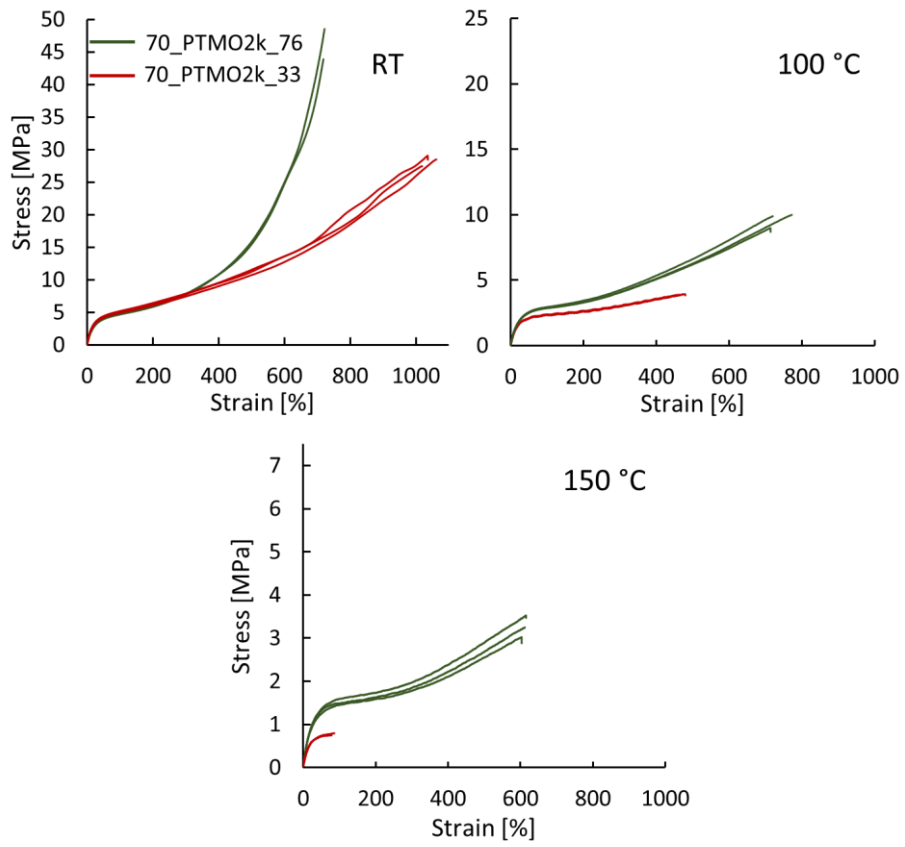


**Figure S3:** Engineering stress-strain curve performed, from left to right, at RT, 100 °C, and 150 °C, at  $\dot{\epsilon} = 0.17 \text{ s}^{-1}$ .

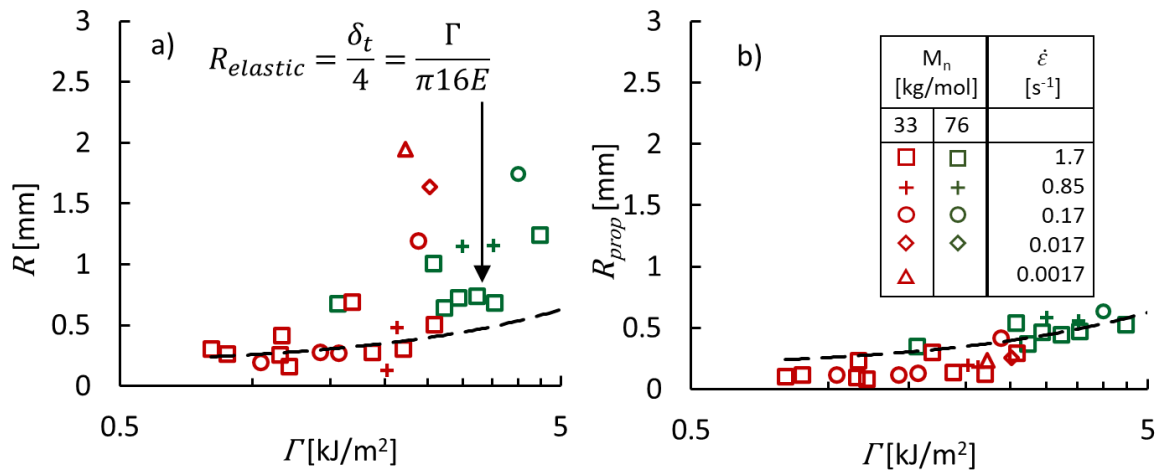


**Figure S4:** Radius of the crack tip right before crack propagation,  $R$ , (a) and during propagation,  $R_{prop}$  (b) calculated via parabolic fit of the crack tip.

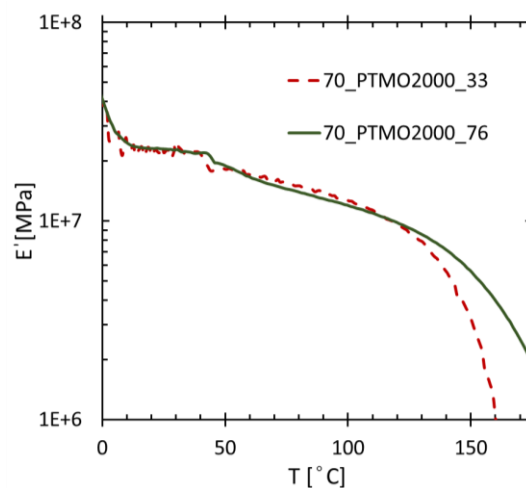


**Figure S5:** Storage modulus of the samples 70\_PTMO2k\_33 and 70\_PTMO2k\_76. Rectangular shaped samples (40 mm long, 2 mm wide) punched out from the 200  $\mu\text{m}$  hot-pressed films are tested in tension at heating rates of 5  $^{\circ}\text{C}/\text{min}$  and at a constant frequency of 1 Hz. The elastic modulus is measured from DMTA rather than being calculated from tensile tests for convenience and increased accuracy.

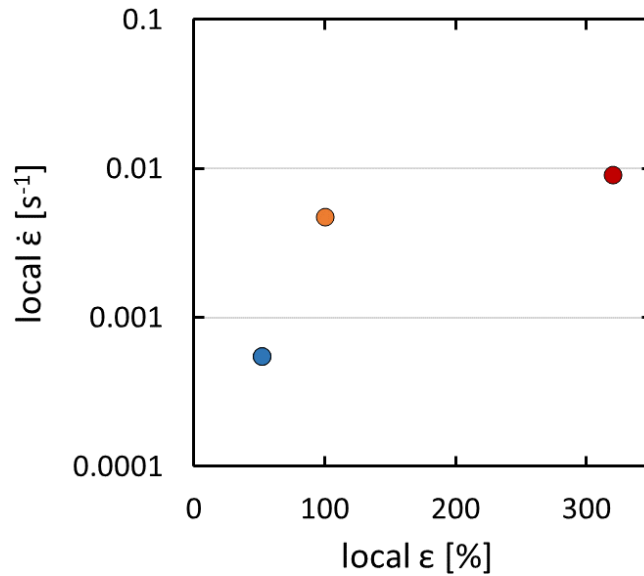


**Figure S6:** Local strain-rate calculated from the changes in the local strain Vs time during the stress relaxation test (Figure 10).

**Derivation of the relationship between  $R_{LEFM}$  and  $\delta_t$**

The equation  $R_{LEFM} = \delta_t / 4$  used in Figure 7 derives from the work of Mac Donald *et al* [54].  $\delta_t$  is determined by the intersection of lines at 45° from the origin of the parabola. The distance between the intersecting line of length  $\delta_t$  and the origin of the parabola is shown to be  $\delta_t / 2$ .

The curvature of the parabola  $y = ax^2$  with origin placed at the crack tip center can be determined by substiting  $y = \delta_t / 2$ ,  $x = \delta_t / 2$ , and  $R_{LEFM} = 1 / |2a|$ .

Substituting and solving for  $R_{LEFM}$  leads to  $R_{LEFM} = \delta_t / 4$ .

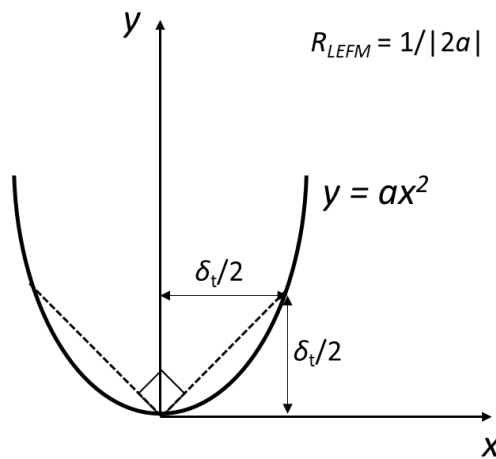


**Table S1-a – Acquired data on PS geometry**

Averages of the failure strain ( $\epsilon_f$ ), failure stress ( $\sigma_f$ ),  $\Gamma$ , and crack-propagation speed ( $v$ ) collected from the tests with notched samples in PS geometry at different T's and  $\dot{\epsilon}$ 's.

Sample	T	$\dot{\epsilon}$	$\epsilon_f$	$\sigma_f$	$\Gamma$	$\Gamma/E$	$\Gamma_{local}$	$v$	
	°C	$s^{-1}$	%	MPa	kJ/m <sup>2</sup>	mm	kJ/m <sup>2</sup>	mm/s	
70_PTMO2k_33	RT	1.7	73.7	4.2	11.9	0.51	6.3	519	
	75	1.7	314.8	1.7	2.2	0.15	1.2	314	
		0.17	206.8	2.7	24.7	1.65	11.3		
	100	1.7	29.7	1.2	1.2	0.09	0.6	243	
		0.85	48.7	1.3	2.1	0.16	1.1	267	
		0.17	39.1	1.1	1.5	0.11	0.8	196	
		0.017	136.1	1.8	12.2	0.94	6.4		
	125	1.7	39.2	1.2	1.1	0.12	0.6	219	
		0.17	54.0	0.8	1.7	0.19	0.9	183	
		0.017	92.1	1.0	3.1	0.34	1.6	295	
		0.0017	65.8	0.8	2.4	0.27	1.3	229	
	70_PTMO2k_76	RT	1.7	81.0	4.3	13.6	0.59	8.5	488
			0.17	231.1	5.2	51.8	2.25	32.4	485
		75	1.7	85.0	3.3	11.5	0.79	7.2	327
			0.17	337.9	4.9	66.7	4.60	41.7	
		100	1.7	72.7	2.9	8.2	0.68	4.2	235
0.85			89.6	2.5	8.0	0.67	2.2	246.	
			330.3	3.9	52.6	4.34	32.9		
0.17			322.3	3.2	47.6	3.93	29.7		
125		1.7	58.4	2.2	3.7	0.41	2.1	167	
		0.85	57.1	1.7	3.3	0.37	2.0	165	
		0.17	427.0	2.9	48.7	5.4	30.5		
150		1.7	47.8	1.2	2.1	0.39	1.4	121	
		0.17	92.1	1.2	5.0	0.92	3.1	124	
		0.017	148.3	1.0	6.9	1.28	4.9	151	
		0.0017	266.7	1.2	13.0	2.40	9.2		

The cells where the crack-propagation value is missing correspond to the experimental conditions at which the crack propagated in the direction perpendicular to the stretching direction, for which the crack-propagation speed was not calculated. The investigated  $\dot{\epsilon}$ 's range from  $0.0017s^{-1}$  to  $1.7s^{-1}$ , however, if at a given  $\dot{\epsilon}$  the crack blunted too much and the crack propagated perpendicularly to the stretching direction, the lower  $\dot{\epsilon}$ 's were not investigated. The uncertainty on the directly measured values are shown in Table S1-b.

**Table S1-b – Uncertainty on the acquired data on PS geometry**

Standard deviation relative to the values shown in Table S1-a.

Sample	T	$\dot{\epsilon}$	$\epsilon_f$	$\sigma_f$	$\Gamma$	$\nu$
	°C	s <sup>-1</sup>	%	MPa	kJ/m <sup>2</sup>	mm/s
70_PTMO2k_33	RT	1.7	1.0	0.4	1.1	9.6
	75	1.7	1.9	0.1	0.4	26.8
		0.17	76.7	0.7	10.7	
	100	1.7	2.9	0.1	0.0	4.1
		0.85	3.2	0.1	0.1	3.9
		0.17	2.3	0.0	0.1	11.9
		0.017	35.5	0.0	3.7	
	125	1.7	8.0	0.4	0.4	19.5
		0.17	23.1	0.0	0.9	46.6
		0.017	29.1	0.2	1.2	11.0
		0.0017	4.2	0.0	0.3	
	70_PTMO2k_76	RT	1.7	14.7	0.4	4.2
0.17			16.4	0.4	0.3	6.1
75		1.7	3.6	0.0	0.9	1.2
		0.17	90.2	0.9	26.8	
100		1.7	13.3	0.3	3.1	7.0
		0.85	170.2	1	31.5	
		0.17	146.3	0.0	25.9	
125		1.7	7.9	0.4	0.8	1.2
		0.85	10.4	0.1	0.4	4.6
		0.17	14.5	0.1	1.9	
150		1.7	7.1	0.2	0.7	17.0
		0.17	8.9	0.2	0.8	1.5
	0.017	4.3	0.0	1.4	3.9	
	0.0017	45.8	0.1	1.7		

**Table S2 – Acquired additional data from standard tensile test**

Averages of the failure strain ( $\epsilon_f$ ), failure stress ( $\sigma_f$ ), yield stress ( $\sigma_y$ ),  $W$ , calculated from the standard tensile tests at different T's and  $\dot{\epsilon}$ 's.

Sample	T	$\dot{\epsilon}$	$\epsilon_f$	$\sigma_f$	$\sigma_y$	$W$
	°C	s <sup>-1</sup>	%	MPa	MPa	MJ/m <sup>3</sup>
70_PTMO2k_33	RT	0.17	1037.7 ± 20.1	28.3 ± 0.8	4.4	136.5 ± 4.7
	75	0.17	655.5 ± 43.1	6.4 ± 0.1	2.7	28.9 ± 2.3
	100	0.17	470.5 ± 12.0	3.9 ± 0.1	2.1	13.0 ± 0.9
		0.017	395.6 ± 46.9	3.3 ± 0.2	1.9	9.6 ± 1.3
		0.0017	338.7 ± 5.9	2.7 ± 0.1	1.7	7.0 ± 0.4
	125	0.17	449.0 ± 36.8	2.2 ± 0.1	1.5	7.8 ± 0.4
70_PTMO2k_76	RT	0.17	713.5 ± 12.0	45.6 ± 3.8	4.0	86.5 ± 4.2
	75	0.17	818.0 ± 103.2	13.7 ± 2.8	2.8	58.3 ± 16.9
	100	0.17	732.7 ± 33.7	9.6 ± 0.6	2.5	38.2 ± 3.0
	125	0.17	618.7 ± 50.8	5.4 ± 0.6	1.9	20.2 ± 3.2
	150	0.17	607.7 ± 6.7	3.2 ± 0.3	1.3	12.3 ± 1.2

As there is no local maximum in the stress-strain curves to represent  $\sigma_y$ , the latter is taken as the stress at  $\epsilon = 50\%$ .  $E_1$  and  $E_2$  are calculated from the cyclic tensile tests as shown in Figure 1. The former corresponds to the unloading modulus calculated from the cycle corresponding to an applied strain of 150%, the latter to the highest applied strain measured.

**Table S3-a – Acquired additional data from cyclic tensile tests**

Averages of  $E_1$  and  $E_2$  calculated from the cyclic tensile tests as shown in Figure 1. The former corresponds to the unloading modulus calculated from the cycle corresponding to an applied strain of 150%, the latter to the highest applied strain measured ( $\epsilon_{max}$ ). The calculation of the moduli takes into account the changes in thickness of the samples with increasing deformation assuming volume conservation.

Sample	T	$E_1$	$E_2(\epsilon_{max})$	$\epsilon_{max}$
	°C	MPa	MPa	%
70_PTMO2k_33	RT	5.8	330.3	550
	75	4.3	65.9	550
	100	2.3	25.1	350
	125	1.0	13.0	350
70_PTMO2k_76	RT	5.5	452.2	550
	75	4.0	211.0	750
	100	3.7	91.0	750
	125	1.2	31.2	450
	150	1.2	16.0	550

## Graphical abstract

We evaluate the failure of industrially relevant soft thermoplastic elastomers at different temperatures, deformation rates, and molecular weights, and link the mechanical and failure behaviors to morphological and molecular structure changes.

